

OrCAS: Origins, Compositions, and Atmospheres of Sub-neptunes. I. Survey Definition

IAN J. M. CROSSFIELD,^{1,2} ALEX S. POLANSKI,^{1,3} PAUL ROBERTSON,⁴ JOSEPH AKANA MURPHY,⁵ EMMA V. TURTELBOOM,⁶ RAFAEL LUQUE,^{7,8} THOMAS BEATTY,⁹ TANSU DAYLAN,¹⁰ HOWARD ISAACSON,⁶ JONATHAN BRANDE,¹ LAURA KREIDBERG,² NATALIE M. BATALHA,⁵ DANIEL HUBER,¹¹ MALEAH RHEM,¹ COURTNEY DRESSING,⁶ STEPHEN R. KANE,¹² MALIK BOSSETT,⁵ ANNA GAGNEBIN,⁵ MAXWELL A. KROFT,⁹ PRANAV H. PREMNATH,⁴ CLAIRE J. ROGERS,⁴ KAREN A. COLLINS,¹³ DAVID W. LATHAM,¹³ CRISTILYN N. WATKINS,¹³ DAVID R. CIARDI,¹⁴ STEVE B. HOWELL,¹⁵ ARJUN B. SAVEL,¹⁶ PERRY BERLIND,¹³ MICHAEL L. CALKINS,¹³ GILBERT A. ESQUERDO,¹³ JESSICA MINK,¹³ CATHERINE A. CLARK,^{17,14} MICHAEL B. LUND,¹⁴ RACHEL A. MATSON,¹⁸ MARK E. EVERETT,¹⁹ JOSHUA E. SCHLIEDER,²⁰ ELISABETH C. MATTHEWS,² STEVEN GIACALONE,^{21,*} THOMAS BARCLAY,²⁰ ROBERTO ZAMBELLI,²² PETER PLAVCHAN,²³ TAYLOR ELLINGSON,²³ MICHAEL BOWEN,²³ GREGOR SRDOC,²⁴ KIM K. MCLEOD,²⁵ RICHARD P. SCHWARZ,¹³ KHALID BARKAOUI,^{26,27,28} JACOB KAMLER,²⁹ FELIPE MURGAS,^{28,30} ENRIC PALLE,^{28,31} NORIO NARITA,^{32,33,28} AKIHIKO FUKUI,^{32,28} HOWARD M. RELLES,¹³ ALLYSON BIERYLA,¹³ ERIC GIRARDIN,³⁴ BOB MASSEY,³⁵ CHRIS STOCKDALE,³⁶ PABLO LEWIN,³⁷ RICCARDO PAPINI,³⁸ PERE GUERRA,³⁹ DENNIS M. CONTI,⁴⁰ SELÇUK YALÇINKAYA,^{41,42} ÖZGÜR BAŞTÜRK,^{41,42} AND GHACHOUI MOURAD⁴³

¹*Department of Physics and Astronomy, University of Kansas, Lawrence, KS, USA*

²*Max-Planck-Institut für Astronomie, Königstuhl 17, D-69117 Heidelberg, Germany*

³*Lowell Observatory, 1400 W. Mars Hill Rd., Flagstaff, AZ, 86001, USA*

⁴*Department of Physics and Astronomy, University of California, Irvine, CA 92697, USA*

⁵*Department of Astronomy and Astrophysics, University of California, Santa Cruz, CA 95060, USA*

⁶*Department of Astronomy, University of California Berkeley, Berkeley, CA 94720, USA*

⁷*Department of Astronomy & Astrophysics, University of Chicago, Chicago, IL 60637, USA*

⁸*NHFP Sagan Fellow*

⁹*Department of Astronomy, University of Wisconsin-Madison, Madison, WI 53706, USA*

¹⁰*Department of Physics and McDonnell Center for the Space Sciences, Washington University, St. Louis, MO 63130, USA*

¹¹*Institute for Astronomy, University of Hawai'i, 2680 Woodlawn Drive, Honolulu, HI 96822, USA; Sydney Institute for Astronomy (SIfA), School of Physics, University of Sydney, NSW 2006, Australia*

¹²*Department of Earth and Planetary Sciences, University of California, Riverside, CA 92521, USA*

¹³*Center for Astrophysics | Harvard & Smithsonian, 60 Garden Street, Cambridge, MA 02138, USA*

¹⁴*NASA Exoplanet Science Institute, IPAC, California Institute of Technology, Pasadena, CA 91125 USA*

¹⁵*NASA Ames Research Center, Moffett Field, CA 94035, USA*

¹⁶*Department of Astronomy, University of Maryland, College Park, College Park, MD 20742 USA*

¹⁷*Jet Propulsion Laboratory, California Institute of Technology, Pasadena, CA 91109 USA*

¹⁸*U.S. Naval Observatory, Washington, D.C. 20392, USA*

¹⁹*U.S. National Science Foundation National Optical-Infrared Astronomy Research Laboratory, 950 N. Cherry Ave., Tucson, AZ 85719, USA*

²⁰*NASA Goddard Space Flight Center, Exoplanets and Stellar Astrophysics Laboratory, Mail Code 667, 8800 Greenbelt Rd, Greenbelt, MD 20771, USA*

²¹*Department of Astronomy, California Institute of Technology, Pasadena, CA 91125, USA*

²²*Societa Astronomica Lunae, Castelnuovo Magra, Italy*

²³*George Mason University, 4400 University Dr, Fairfax, VA 22030*

²⁴*Kotizarovci Observatory, Sarsoni 90, 51216 Viskovo, Croatia*

²⁵*Department of Physics and Astronomy, Wellesley College, Wellesley, MA 02481, USA*

²⁶*Astrobiology Research Unit, Université de Liège, 19C Allée du 6 Août, 4000 Liège, Belgium*

²⁷*Department of Earth, Atmospheric and Planetary Science, Massachusetts Institute of Technology, 77 Massachusetts Avenue, Cambridge, MA 02139, USA*

²⁸*Instituto de Astrofísica de Canarias (IAC), Calle Vía Láctea s/n, 38200, La Laguna, Tenerife, Spain*

²⁹*John F. Kennedy High School, 3000 Bellmore Avenue, Bellmore, NY 11710, USA*

³⁰*Departamento de Astrofísica, Universidad de La Laguna (ULL), E-38206 La Laguna, Tenerife, Spain*

³¹*Departamento de Astrofísica, Universidad de La Laguna (ULL), 38206, La Laguna, Tenerife, Spain*

³²*Komaba Institute for Science, The University of Tokyo, 3-8-1 Komaba, Meguro, Tokyo 153-8902, Japan*

³³*Astrobiology Center, 2-21-1 Osawa, Mitaka, Tokyo 181-8588, Japan*

³⁴*Grand Pra Observatory, 1984 Les Hauderes, Switzerland*

³⁵*Villa '39 Observatory, Landers, CA 92285, USA*

³⁶*Hazelwood Observatory, Australia*

³⁷*The Maury Lewin Astronomical Observatory, Glendora, California. 91741. USA*

³⁸*Wild Boar Remote Observatory, San Casciano in val di Pesa, Firenze, 50026 Italy*

³⁹*Observatori Astronòmic Albanyà, Camí de Bassegoda S/N, Albanyò 17733, Girona, Spain*

⁴⁰*American Association of Variable Star Observers, 185 Alewife Brook Parkway, Suite 410, Cambridge, MA 02138, USA*

⁴¹*Ankara University, Faculty of Science, Astronomy and Space Sciences Department, Tandogan, TR-06100, Ankara, Türkiye*

⁴²*Ankara University, Astronomy and Space Sciences Research and Application Center (Kreiken Observatory), Alper Gezeravcı Yerleşkesi, İncek Blvd., TR-06837, Ahlatlıbel, Ankara, Türkiye*

⁴³*Oukaimeden Observatory, High Energy Physics and Astrophysics Laboratory, Cadi Ayyad University, Marrakech, Morocco*

ABSTRACT

Sub-Neptunes — volatile-rich exoplanets smaller than Neptune — are intrinsically the most common type of planet known. However, the formation and nature of these objects, as well as the distinctions between sub-classes (if any), remain unclear. Two powerful tools to tease out the secrets of these worlds are measurements of (i) atmospheric composition and structure revealed by transit and/or eclipse spectroscopy, and (ii) mass, radius, and density revealed by transit photometry and Doppler spectroscopy. Here we present *OrCAS*, a survey to better elucidate the origins, compositions, and atmospheres of sub-Neptunes. This radial velocity survey uses a repeatable, quantifiable metric to select targets suitable for subsequent transmission spectroscopy and address key science themes about the atmospheric & internal compositions and architectures of these systems. Our survey targets 26 systems with transiting sub-Neptune planet candidates, with the overarching goal of increasing the sample of such planets suitable for subsequent atmospheric characterization. This paper lays out our survey’s science goals, defines our target prioritization metric, and performs light-curve fits and statistical validation using existing *TESS* photometry and ground-based follow-up observations. Our survey serves to continue expanding the sample of small exoplanets with well-measured properties orbiting nearby bright stars, ensuring fruitful studies of these systems for many years to come.

1. INTRODUCTION

Precise elemental and molecular abundance measurements provide some of the strongest constraints on the formation and evolution of planets, stars, and galaxies. In the coming decades, such measurements will also inform the search for extrasolar biosignatures. JWST is now the superlative platform for exoplanet characterization because it allows us to finally measure precise atmospheric abundances (e.g., [JTEC Team et al. 2023](#); [Madhusudhan et al. 2023](#); [Bell et al. 2023](#); [Beatty et al. 2024](#)). To provide a clearer understanding of planet formation, composition, and chemistry, we must build a complete, homogeneous sample of planetary abundances across wide swaths of parameter space and link together the compositions of exoplanets, their host stars, and the Solar system.

Sub-Neptunes and super-Earths occur more frequently than any other type of known exoplanet, making these bodies the most common end product of the process of planet formation (Fig. 2a; [Howard et al. 2010](#);

[Fulton et al. 2017](#)). Although in general sub-Neptunes are larger and more volatile-rich than super-Earths, it is challenging to discriminate the two classes based on transit-derived properties alone. Thus although our work targets the more H/He-rich sub-Neptunes, some smaller, denser super-Earths may also make it into our sample. For either of these planet types, observing the planets’ atmospheres provides one of the best hopes for determining formation history, and the *only* hope for understanding the interplay between initial composition and present-day chemistry, dynamics & circulation, and disequilibrium processes ([Bowler 2016](#); [Deming & Seager 2017](#)). Models of planet formation for sub-Neptunes can be directly tested via JWST measurements of atmospheric composition, but to make the greatest impact precise ($\geq 5\sigma$) masses are needed to prevent mass uncertainties from dominating the error budgets of atmospheric retrievals ([Batalha et al. 2019](#)).

Furthermore, precise planet masses are a looming, underappreciated bottleneck for JWST. According to

* NSF Astronomy and Astrophysics Postdoctoral Fellow

the NASA Exoplanet Archive¹, over two thousand sub-Neptunes are known but only 167 have 5σ masses; of those, only 81 are good targets for atmospheric characterization ($TSM^2 > 30$). JWST (and soon, ARIEL) need hundreds more such planets if they are to successfully survey large numbers of exoplanet atmospheres. Confirming these planets via precise RV masses, and preparing for atmospheric spectroscopy, is the primary (though not sole) focus of our program.

This program is OrCAS: an RV survey to inform our understanding of the Origins, Compositions, and Atmospheres of Sub-neptune exoplanets. By using modern RV facilities such as WIYN/NEID (Schwab et al. 2016) and Keck/KPF (Gibson et al. 2016) the program aims to provide a large number (up to 26) of sub-Neptunes with precise masses, in order to support subsequent JWST and ARIEL atmospheric characterization of a large and demographically-representative sample of these intrinsically-common planets. In addition, our program will characterize stellar activity in known planet-hosting systems, explore system architectures, and determine precise planet densities and bulk compositions. OrCAS currently obtains its observations with Keck/KPF (Gibson et al. 2016) through a four-semester NASA Keck Strategic Mission Support program (KSMS), and with WIYN/NEID (Schwab et al. 2016) through allocations from NOIRLab and the University of Wisconsin-Madison (UW-Madison).

Given the heady success of TESS at finding new planets that are subjected to subsequent characterization, naturally ours is far from the only effort focusing on sub-Neptune characterization. A non-exhaustive list of these includes the PFS Magellan-TESS Survey (Teske et al. 2021), the HIRES TESS-Keck Survey (Chontos et al. 2022; Polanski et al. 2024), the HARPS NCORES survey (Armstrong et al., in review), and more.

This paper defines the OrCAS survey, and is written in the same spirit as Teske et al. (2021) and Chontos et al. (2022); our first results and mass measurements, for TOI-6054/HD 23074, are presented in Paper II (Kroft et al., in prep.). Here we present our science goals, rigorously describes our approach to target selection, and provides transit fits and statistical validation of our target sample.

2. SCIENCE THEMES

Here we present the four main science themes of our program. The primary and driving goal (Theme I,

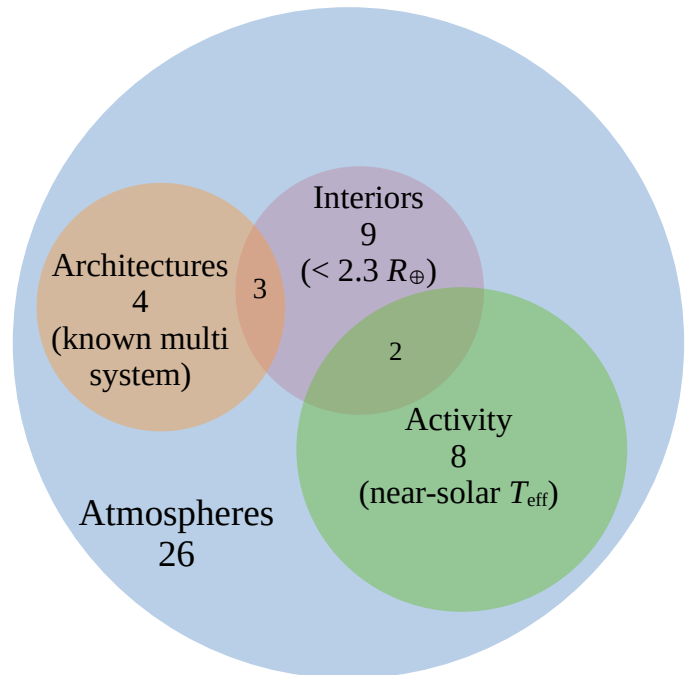


Figure 1. Number of target systems in each of our science themes: atmospheres (I), interior compositions (II), system architectures (III), and stellar activity (IV). See Sec. 2 and Table 1 for details.

Sec. 2.1 below) is to enable many more future sub-Neptune atmospheric measurements by obtaining $\geq 5\sigma$ RV planet masses. Table 1 and Fig. 1 show the breakdown of which targets fall under which science theme.

2.1. Theme I: Atmospheres

Volatile elements such as C and O have long been observed in exoplanet atmospheres (e.g., Konopacky et al. 2013), and refractory elements have also been recently measured in hot Jupiters (e.g., Lothringer et al. 2021; Tsai et al. 2023; Sing et al. 2024; Welbanks et al. 2024). JWST is finally beginning to allow us to extend these compositional analyses to reveal the makeup and formation pathways of sub-Neptunes (Madhusudhan et al. 2023; Crossfield 2023; Beatty et al. 2024).

Fundamentally, measuring atmospheric compositions of sub-Neptunes requires atmospheric spectroscopy – and thus also requires precise masses ($\leq 20\%$ fractional precision) to enable that spectroscopy (Batalha et al. 2019). With JWST’s unprecedented sensitivity, constraints on atmospheric composition are finally precise enough to begin to test the quantitative predictions of planet formation models.

For example, early JWST transmission spectroscopy of K2-18b highlights the sub-Neptune atmospheric science now enabled by JWST (Madhusudhan et al. 2023). These spectra revealed CH_4 and CO_2 and show that

¹ <https://exoplanetarchive.ipac.caltech.edu/>

² (Transmission Spectroscopy Metric, a proxy for the S/N of JWST transmission spectroscopy; Kempton et al. 2018).

Table 1. Stellar Parameters (from TIC):

TOI	TIC	Names	RA [°]	Dec [°]	V [mag]	T_{eff} [K]	R_* [R_{\odot}]	M_* [M_{\odot}]	Theme	n_{sectors}
1174	154089169	TYC 4403-2080-1	209.217175	+68.618211	10.96	5030± 60	0.760±0.050	0.85±0.10	1	10
1180	158002130	TYC 4565-656-1	214.555774	+82.193764	11.02	4738±139	0.730±0.050	0.75±0.09	1	14
1184	233087860	TYC 4201-1875-1	272.20452	+60.678785	10.99	4534±128	0.690±0.060	0.71±0.08	1	31
1244	219850915	TYC 4421-473-1	256.279559	+69.519093	11.93	4599±123	0.721±0.053	0.73±0.09	1	29
1247	232540264	HD135694, HIP74326	227.867864	+71.841296	9.08	5712±106	1.080±0.050	1.02±0.12	1 4	16
1301	356867115	TYC 4437-668-1	275.862543	+71.581748	11.34	4820± 32	0.732±0.048	0.77±0.09	1 3	30
1467	240968774	LP 151-22, NLTT4212	19.114644	+49.233138	12.29	3834±157	0.491±0.015	0.489±0.020	12	3
1630	317597583	BD+74 1020	352.016676	+75.552607	9.62	5504±130	0.830±0.040	0.95±0.13	1	7
1659	288631580	BD+82 553	277.925194	+82.305949	10.08	5977±131	1.006±0.048	1.10±0.14	12 3	16
1691	268334473	BD+86 279	272.404118	+86.860343	10.13	5759±187	1.000±0.050	1.03±0.14	1 4	11
1716	14336130	HD237566	105.083329	+56.824194	9.41	5879±141	1.240±0.070	1.07±0.14	1 4	4
1723	71431780	BD+68 495	116.797198	+68.476685	9.66	5777±125	1.090±0.050	1.04±0.13	1 4	5
1739	159418353	LP 8-221, NLTT42078	240.172481	+83.258659	10.69	4814±125	0.781±0.054	0.78±0.09	12	15
1744	229455001	BD+60 1982	294.291071	+60.881302	9.54	6179±125	1.140±0.050	1.18±0.16	1	30
1758	367858035	TYC 4602-357-1	354.741581	+75.685232	10.79	5169±122	0.810±0.050	0.88±0.11	1	7
1768	137906197	TYC 3818-1387-1	152.102783	+55.53996	10.42	5994±121	1.100±0.050	1.10±0.15	1	4
1772	85293053	BD+35 2144	156.837704	+34.39095	9.96	5583±110	0.995±0.046	0.99±0.13	1 3	2
1777	29191624	HD87620, HIP49576	151.807032	+46.114881	9.31	5859±102	0.980±0.040	1.06±0.13	12 4	2
1782	160045097	UCAC4 823-018203	213.078772	+74.411791	12.33	4336±121	0.669±0.056	0.68±0.08	12 3	11
1798	198153540	TYC 3465-1049-1	211.093937	+46.519283	11.36	5165±104	0.780±0.040	0.87±0.11	12 3	6
1799	8967242	HD96735, HIP54491	167.232915	+34.303015	8.98	5690±123	0.957±0.046	1.01±0.13	12 4	2
2211	212253390	HD195755, HIP101503	308.539086	-29.672613	9.99	5253±123	0.834±0.047	0.90±0.11	12	2
4638	58824746	TYC 611-390-1	12.820663	+12.787986	11.66	5700±131	0.895±0.044	1.02±0.13	1 4	3
5726	71582156	BD+69 458	123.39505	+68.57459	9.74	5874±119	1.106±0.051	1.06±0.13	1 4	5
5799	328081248	NLTT48731, G 143-29	301.630179	+15.989142	13.29	3521±157	0.343±0.010	0.327±0.020	12	1
6054	392681545	HD23074, HIP17540	56.337007	+60.350917	8.02	6112±119	1.612±0.070	1.15±0.16	1 3	1

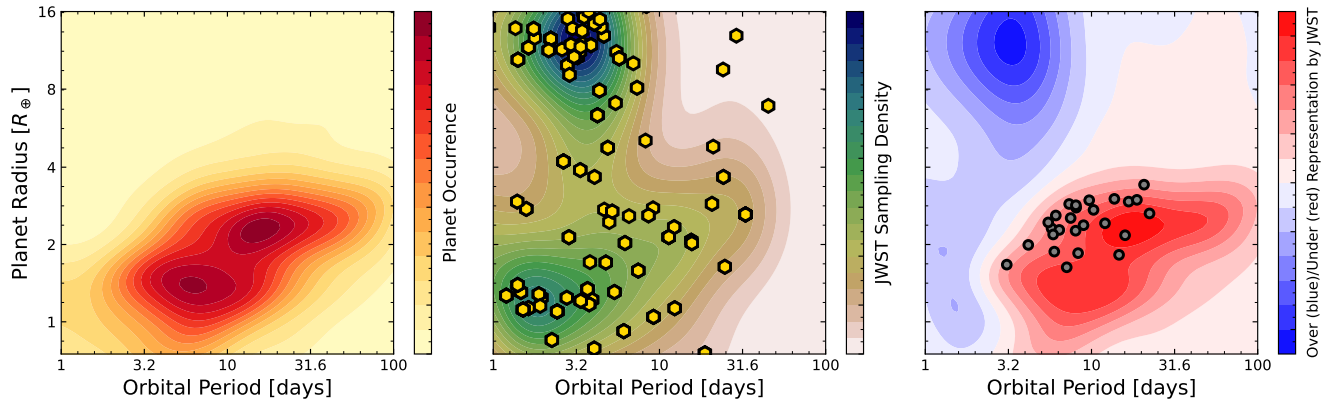


Figure 2. Target prioritization. *Left:* Planet occurrence rate (Fulton & Petigura 2018), showing that sup-Neptunes and super-Earths are the most common planets on short-period orbits. *Center:* Gold hexagons show transiting exoplanets targeted by JWST in Cycles 1 & 2 (our survey began before Cycle 3 results were announced); the shading is a Kernel Density Estimate map showing that hot Jupiters and super-Earths were the most commonly targeted planets. *Right:* Difference of the two heat maps, showing that temperate sub-Neptunes (red region) remain underrepresented by JWST relative to the intrinsic underlying population. We identified our targets (gray points) by weighting by this under-representation, TSM, and observing efficiency (see text for details).

JWST is capable of efficiently producing high-precision measurements even for small planets. The measured abundances for the identified species are far more precise than was feasible with HST, with JWST breaking key model degeneracies (e.g., between H_2O and CH_4). Such tight constraints on atmospheric composition would not be possible without the 5.4σ planet mass constraint obtained from RV observations (Cloutier et al. 2019; Radica et al. 2022).

However, JWST is rapidly running out of small transiting planet targets. In its first three Cycles, JWST will characterize 133 transiting exoplanets, from hot Jupiters to cool rocky worlds (Fig. 2b). If JWST operates for 20 years then the mission could characterize the atmospheres of nearly a thousand exoplanets during its lifetime. Such a large survey may be necessary to beat down the stochasticity of planet formation and finally enable population-level studies linking atmospheres to planet size, mass, orbits, and host star properties. To best investigate the smaller sub-Neptunes that are the most common end-products of planet formation, most of JWST’s effort should focus on these intrinsically common worlds. However, sub-Neptunes are extremely underrepresented in JWST’s target pool, especially compared to intrinsic occurrence rates (Fig. 2).

Furthermore, JWST’s accessible, small-planet sample could be exhausted in just \sim two more cycles (leaving none for ARIEL; Tinetti et al. 2018) unless additional sub-Neptune masses can be measured. Though there are currently 94 known planets with $R_p < 4R_\oplus$, high TSM, and a $>5\sigma$ mass, JWST is observing 56 planets with $R_p < 4R_\oplus$ in Cycles 1–3. As described below, our new TESS-discovered systems will be excellent targets for future GO programs to explore the atmospheres of sub-Neptune exoplanets.

Completing a demographic assay of sub-Neptune atmospheres will take years and require a much larger sample of sub-Neptunes with precise masses. Efforts to date (mainly with HST) have been suggestive of trends of cloud properties with equilibrium temperature (e.g., Brande et al. 2024), but it remains unclear whether these conclusions are consistent with recent JWST results (e.g., Wallack et al. 2024; Alderson et al. 2024; Beatty et al. 2024, and others). A larger number of deep, sensitive, JWST observations are urgently needed. Above all else, our program’s measurement of these new sub-Neptune masses from $1.6\text{--}4.2 R_\oplus$ and T_{eq} from 400–1200 K (Fig. 4) aims to support the burgeoning field of sub-Neptune atmospheric characterization.

2.2. Theme II: Internal Compositions

Radius alone is not sufficient to infer even an approximate internal composition for sub-Neptunes, since the bulk makeup of these planets becomes highly degenerate between rock, ice, and H_2/He (Adams et al. 2008; Figueira et al. 2009). Furthermore, masses of the sub-Neptune population can vary by up to a factor of 5 for a given radius implying a compositional diversity not reflected by single-valued mass-radius relations (Wolfgang et al. 2016; Otegi et al. 2020; Parviainen et al. 2024). Systems such as TOI-849 ($3.5 R_\oplus$ with a mass of $39 M_\oplus$; Armstrong et al. 2020) and TOI-1853 ($3.5 R_\oplus$, but a whopping $73 M_\oplus$; Naponiello et al. 2023) demonstrate that in the sub-Neptune population, both radius and mass are needed to reliably infer density and surface gravity, and to begin to infer bulk planetary composition.

With precise masses from Doppler spectroscopy and refined radii from transit analyses, derived measurements of bulk density can contribute to population-level searches for demographic trends. Such measurements also serve to constrain planets’ core mass fractions and elemental compositions, and provide hints about how and where they formed (Luque & Pallé 2022). For example, rocky and giant planets are expected to form within and beyond the frost line, respectively, whereas water worlds may have formed outside the frost line but have migrated inward since formation. TESS has observed numerous transits of most of our sample (see Table 1), enabling precise radius measurements of our planet candidates (see Sec. 4).

Recent RV and transit surveys suggest that below $\lesssim 2R_\oplus$, the super-Earth/sub-Neptune dichotomy may actually be a trichotomy of rocky, icy, and gaseous small planets orbiting cooler M dwarfs (Luque & Pallé 2022). Probing the nuances of this region of the mass-radius diagram has largely been inhibited by a lack of precise mass measurements (especially for planets around hotter, more massive stars). More data points are needed to explore this part of mass-radius space in finer detail (Parc et al. 2024), and to determine whether the compositional model of Luque & Pallé (2022) extends to planets orbiting stars hotter than M dwarfs (Rogers et al. 2023).

More broadly, there is considerable interest in measuring the shape and intrinsic scatter of the exoplanetary mass-radius relation. By providing an objective, reproducible target prioritization metric (see Sec. 3) we aim to allow our mass and radius measurements to be incorporated into future efforts, e.g. using hierarchical Bayesian modeling and non-parametric mass-radius relations (Wolfgang et al. 2016; Ning et al. 2018; Kanodia et al. 2019, 2023), with minimal selection bias effects.

2.3. Theme III: System Architectures

Sub-Neptunes are observed to be the most commonly-occurring product of planet formation (e.g., [Fulton & Petigura 2018](#)); their orbital architectures and atmospheres are complementary fossils of their formation and migration histories. For example, when planets smoothly migrate through their natal disk the systems may remain flat, densely-packed, and dynamically ‘cool,’ while systems that evolved by planet-planet scattering may become more widely spaced and dynamically ‘hot.’ Measuring the planet multiplicity, orbital eccentricity, and spin-orbit alignment (obliquity) constrains these pathways ([Winn & Fabrycky 2015](#)).

Measuring the masses of multiple planets in a single system enables comparative atmospheric characterization, e.g. by controlling for the unknown X-ray and UV irradiation history as well as our imprecise knowledge of stellar age and abundances ([Owen 2019](#); [Libby-Roberts et al. 2020](#)). By providing precise mass measurements of all known planets in multi-planetary systems, we aim to deliver cosmic laboratories amenable to atmospheric studies of multi-planet systems.

Modern RV follow-up of TESS planets also serves to bring Kepler-era results into the TESS era — for example, testing for “Peas in a Pod” (e.g., [Weiss et al. 2018](#)) by comparing orbits, sizes, masses, and eccentricities of our sample; using long-baseline RVs to test the “Edge-of-the-multis” claim that multi-planet systems appear truncated relative to detection limits ([Millholland et al. 2022](#)); and allowing an independent, RV-driven test of the eccentricity peak seen at $2 R_{\oplus}$ in Kepler systems ([Gilbert & Petigura 2024](#)). Our long RV baseline ($\gtrsim 2$ yrs) and high precision will likely reveal additional non-transiting and/or long-period companions, whose discovery will improve the interpretation of these systems. Such long-term RV studies reveal, e.g., the connection between the formation of short-period sub-Neptunes and cold gas giant planets on orbits more like those found in our own solar system (e.g., [Bonomo et al. 2023](#); [Bitsch & Izidoro 2023](#)). Precise masses and Keplerian orbits will improve dynamical stability modeling of our targets, providing evidence for companions or resonances, as well as determining regions where dynamically stable orbits are excluded.

Finally, precise RVs can also measure the sky-projected obliquity between a planet’s orbital and its star’s rotational axes via the Rossiter-McLaughlin (RM) effect. A large spin-orbit misalignment may be indicative of secular gravitational interactions with an outer companion ([Winn 2010](#); [Bourrier et al. 2021](#)). Whether by measuring our targets’ masses or (in later programs) measuring orbital obliquities, our validated sample will

enable the confirmation of these candidates as true planets and facilitate later atmospheric studies of these worlds.

2.4. Theme IV: Stellar Activity

With next-generation Doppler spectrometers, the chief RV limitation is often astrophysical noise arising from variable stellar surfaces. Developing improved techniques for diagnosing and mitigating this stellar “jitter” is a critical requirement for the extreme-precision radial velocity (EPRV) community to achieve its near- and long-term goals ([Crass et al. 2021](#)) of measuring masses of transiting planets for atmospheric study ([Batalha et al. 2019](#)), and identifying targets for NASA’s Habitable Worlds Observatory (HWO; [Luhn et al. 2023](#)). High-precision RV surveys provide legacy data sets that are immensely valuable for testing strategies for identifying and removing RV jitter around a broad range of stellar types using cutting-edge data.

Several aspects of our experimental design will make the resulting time-series data ideal for developing techniques to mitigate astrophysical noise. Our targets are all transiting systems, which “freezes” the planetary periods and ephemerides and simplifies the challenge of modeling planets and jitter simultaneously. Furthermore, the TESS discovery light curves provide additional information on the variability driving jitter, since even non-contemporaneous space-based light curves help predict and correct for RV jitter ([Aigrain et al. 2012](#); [Bastien et al. 2013](#); [Beard et al. 2024](#)). The broad wavebands, intrinsic stability, and high resolution, of modern spectrographs allow for the extraction of a diverse set of stellar activity tracers, such as absorption-line indicators (Ca II H&K, H α , Ca IR triplet), line-shape deformation metrics ([Zechmeister et al. 2018](#)), and chromatic dependence of signal amplitudes ([Cale et al. 2021](#)). The high S/N achieved is especially important for “line-by-line” RV extractions, which minimize jitter by excluding activity-sensitive absorption lines (e.g. [Cretignier et al. 2023](#); [Ould-Elhkim et al. 2023](#)).

We expect that several of our targets will ultimately require intensive activity modeling to obtain robust planetary masses. This activity challenge is an opportunity to use precise RV data to refine jitter mitigation techniques and push the limiting exoplanet detection sensitivity down to the level of intrinsic instrumental noise floors. This work will support future EPRV efforts to seek all kinds of planets – including small, rocky, temperate HWO targets orbiting Sun-like stars – especially since our target T_{eff} distribution closely mirrors the HWO target list ([Mamajek & Stapelfeldt 2024](#)).

3. TARGET SELECTION, VETTING, AND VALIDATION

3.1. Target Selection

We designed our program to have a well-defined, repeatable target selection process in order to facilitate subsequent, minimally-biased population-level studies. The primary consideration in designing the sample and associated prioritization metrics was the goal of expanding the pool of sub-Neptunes with $\geq 5\sigma$ masses so that future JWST and ARIEL atmospheric spectroscopy can focus on a planet sample more generally representative of underlying demographic trends (cf. Fig. 2).

To prioritize our targets, we considered all TOIs as of September 2023 and followed the steps below. First, we took the intrinsic short-period planet occurrence distribution (Fulton & Petigura 2018). Since the underlying period-radius distribution from that work was not available from the authors (B. Fulton, priv. comm.) we constructed our own proxy for the intrinsic occurrence rate as follows. We took the merged list of physical parameters from the California-Kepler Survey (Petigura et al. 2017; Johnson et al. 2017) then followed an analogous set of steps as that described by Fulton & Petigura (2018): specifically, selecting only those systems with impact parameter $b < 0.7$, period $P < 100$ d, stellar radii $R_* < 2.1R_\odot$, stellar T_{eff} between 4700–6500 K, and finite planet radii. This results in the period-size distribution shown in Fig. 2a, which closely resembles the corresponding distribution of Fulton & Petigura (2018).

We then constructed a Kernel Density Estimate (KDE) map from the approved JWST Cycle 1 and 2 transiting exoplanet sample (green shading in Fig. 2b). The difference between these two maps shows which types of planets are over- or under-represented (blue and red regions, respectively, in Fig. 2c) in JWST’s target list relative to intrinsic occurrence rates. We dub this the Sub-neptune Under-representation Rate (SUR). Each of the three color maps in Fig. 2 is available in electronic form, to facilitate reproduction of our analysis.

For each potential target, we then estimated the necessary number of RV observations (and the total observing time) to reach a 5σ mass. Although OrCAS radial velocity spectra are being obtained from a variety of sources, to ensure a homogeneous, repeatable, and straightforward target selection metric we must select a single instrument to use for these calculations. Since our largest observing award consists of Keck/KPF time, we used the KPF exposure time calculator³ to estimate

the observing time required. We assumed an internal KPF noise floor of 0.5 m s^{-1} (KPF Instrument Team, priv. comm.) and added estimated stellar RV noise from granulation & oscillation (following Yu et al. 2018) and rotation (Galland et al. 2005). We used the candidates’ radii to estimate their masses and RV semi-amplitudes via the simple, invertible, single-valued power-law relation $M_P = R_P^{2.06}$ (in Earth units; Lissauer et al. 2011). Then we compared the total estimated per-shot RV uncertainty σ_1 (obtained by adding the expected instrumental and astrophysical noise sources in quadrature) to the TOI’s estimated RV semi-amplitude, K , estimating a minimum number of RVs needed to reach a 5σ mass as $(5/(K/\sigma_1))^2$.

Our experience shows that for such small RV signals, and for these smaller planets (which are frequently in multi-planet systems with other non-transiting companions), we must obtain a minimum of $\gtrsim 30$ RVs per target (see also Akana Murphy et al. 2024). Furthermore, since programs that stop observations after achieving a preset significance threshold (e.g., 5σ) result in upwardly biased masses (Burt et al. 2018) we therefore plan to obtain a minimum of 30 RVs for all targets; this choice should also help to minimize bias in our final mass sample (cf. Teske et al. 2021; Chontos et al. 2022). Since the performance of KPF is still evolving, in the final survey we may elect to obtain a larger number of RVs for a smaller subset of targets.

Our final prioritization metric M is then the SUR (Fig. 2c) of each target’s radius and period, multiplied by each target’s TSM, divided by the estimated time to measure a 5σ mass for that planet:

$$M = \text{SUR}(R_p, P) \times \text{TSM}(R_p, M_p, a, R_*, T_{\text{eff}}, m_J) / t_{5\sigma}. \quad (1)$$

We settled on this choice in order to access not simply the best overall targets for atmospheric study, but merely targets of reasonably high quality whose masses were not unduly expensive to measure. Finally, we also required all targets to have $\text{TSM} \geq 30$ and $J > 6$ mag to allow precise JWST constraints without wholly saturating the useful instrument modes, and declination $> -20^\circ$ (to ensure targets that are accessible from northern-hemisphere observatories such as KPF and NEID). This final step left us with a list of roughly 100 rank-ordered TOIs. A Python software tool to generate our prioritized target list, along with SUR values, is available online at <https://github.com/iancrossfield/OrCAS.target.selection>.

3.2. Target Vetting and Validation

To ensure that observatory resources are well-utilized, we comprehensively vetted all of these ~ 100 prioritized

³ <https://github.com/California-Planet-Search/KPF-etc>

TOIs. We used the TESS Exoplanet Follow-up Observing Program (ExoFOP) website to vet our potential targets. We removed all targets where: ground-based time-series photometry (SG1, see Appendix A) revealed that the transit occurs around a fainter, nearby star; where single-epoch recon spectroscopy (SG2) revealed secondary lines, large RV shifts indicative of stellar companions, very high activity ($R'_{\text{HK}} > -4.5$), or $v \sin i > 7 \text{ km s}^{-1}$; where high-resolution imaging (SG3, see Appendix B) revealed nearby stellar companions that could actually host the transit signal or that would be blended with the target star in the KPF aperture; where targets were already being intensively followed up by precise RV campaigns (SG4); and where the TESS project's photometric vetting plots indicated significant secondary eclipses, off-target transits, or coherent photometric variability of $>0.1\%$. These checks led us to exclude the following TOIs from our sample: 1154.01, 1262.01, 1277.02, 1287.01, 1404.01, 1430.01, 1432.01, 1434.01, 1437.01, 1438.02, 1440.01, 1441.01, 1443.01, 1445.01, 1451.01, 1453.01, 1464.01, 1473.01, 1643.01, 1648.01, 1730.01, 1730.03, 1735.01, 1736.01, 1740.01, 1742.01, 1751.01, 1778.01, 1801.01, 1802.01, 1824.01, 1835.01, 2280.01, 2287.01, 4576.01, 5076.01, 5117.01, 5156.01, 5515.01, and 5539.01.

We then statistically validated our remaining 29 target planet candidates using the public TRICERATOPS tool (Giacalone et al. 2021), which calculates the false positive and nearby false positive probabilities (FPP/NFPP) of each candidate transit signal. Such validation analyses attempt to rule out astrophysical false positive scenarios such as eclipsing binaries and have been employed since the Kepler era (Borucki et al. 2012). We begin by pulling each TOI's SPOC-processed light curve (Jenkins et al. 2016) from the MAST database using Lightkurve (Lightkurve Collaboration et al. 2018). The apertures used in the initial TESS alert pipeline are also used as input to TRICERATOPS, as is existing high-resolution imaging data (downloaded from the public ExoFOP website, where available; see Appendix B). To reliably estimate the FPP and NFPP, we run TRICERATOPS 20 times per candidate planet. Giacalone et al. (2021) recommends that after vetting, candidates be assigned a disposition of validated planet (VP; $\text{FPP} < 0.015$ and $\text{NFPP} < 10^{-3}$), likely planet (LP, $\text{FPP} < 0.5$ and $\text{NFPP} < 10^{-3}$), or likely nearby false positive ($\text{NFPP} > 0.1$).

Our TRICERATOPS analysis identified three potential targets as having a high likelihood of being nearby false positives. These TOIs (and their FPP and NFPP values) are: 1432.01 (0.14 ± 0.03 and 0.11 ± 0.02), 1643.01 (0.32 ± 0.15 and 0.27 ± 0.10), and 4576.01 (0.70 ± 0.30 and

0.70 ± 0.30). We therefore removed these systems from our sample, leaving our final sample of 26 targets described in Tables 1 and 2. The total sum of FPP and NFPP values across our selected target sample is just 0.17, indicating only a roughly one-in-six chance of having even a single target turn out to be a false positive. In addition to these 26 targeted sub-Neptunes, three systems with multiple transiting planet signals (TOI-1782, TOI-1798, and TOI-6054/HD 23074) bring the total number of known planets in our sample to 31.

Note that although we removed potential targets being extensively observed by high-precision Doppler spectroscopy, we elected to keep targets being intensively observed by Keck/HIRES. This is because the RV precision of HIRES is somewhat lower than modern RV spectrographs, sometimes preventing it from measuring the low masses expected for much of our sample. Indeed, although HIRES mass measurements were recently reported for 13 planets (including 12 in our selected sub-Neptune sample) in Table 2, none of the selected sub-Neptune targets rise above a significance level of 3.5σ (Polanski et al. 2024). The ultra-short-period planet TOI-1798.02 has a significant mass measurement of $5.6^{+0.8}_{-0.7} M_{\oplus}$ (Polanski et al. 2024), but we include this target here only because its companion, TOI-1798.01, is a sub-Neptune selected by our prioritization metric.

4. UNIFORM DETERMINATION OF PLANET RADII

To derive system parameters (including transit depths and planet radii) for our targets, we fit light curve models to the *TESS* photometry using the same software and approach as Crossfield et al. (2015, 2016). Although ground-based time-series photometry exists for some targets (see Appendix A), we opt to use a homogeneous, *TESS*-only analysis to characterize our targets' transits. We used all 120-second cadence, PDC-SAP *TESS* photometry available for each target as of May 2024, accessing the data series with Lightkurve (Lightkurve Collaboration et al. 2018). Table 1 lists the number of sectors of *TESS* data (as of mid-2024), n_{sectors} , used to analyze each system. We trimmed each light curve to include only those points within $\pm 2.5 T_{14}$ of the estimated transit mid-center, reducing the data volume (and computational time) by roughly 90%. We use stellar parameters and associated uncertainties from the TESS Input Catalog (TIC) v8.2 (Stassun et al. 2018), and used LDTK (Parviainen & Aigrain 2015) to set Gaussian priors on the quadratic limb-darkening coefficients by using the uncertainties on the stellar parameters. Although we used the TIC to ensure homogeneous and repeatable target selection, subsequent analyses of

individual systems will provide updated and refined stellar parameters, as well as bespoke transit analyses of all systems.

Our analysis fits for transit mid-center T_0 , orbital period P , orbital inclination i , the ratios R_P/R_* and R_*/a , the quadratic limb-darkening coefficients, and an overall multiplicative scaling constant. The light-curve analysis begins with an initial guess defined by the TOI parameters from the TESS project, followed by alternating applications of an optimizer (the SciPy downhill simplex algorithm, `optimize.fmin` Virtanen et al. 2020) and a Markov-Chain Monte Carlo (MCMC) sampler (`emcee`; Foreman-Mackey et al. 2013). `BATMAN` (Kreidberg 2015) is used to model the light curves. The analysis restarts when an improved fit is found, and concludes after either 20,000 steps or when the Gelman-Rubin metric for all parameters is < 1.03 . The final light-curve fits are shown in Fig. 3 and the resulting parameters and uncertainties are listed in Table 2.

5. TARGET SAMPLE & OBSERVING STRATEGY

5.1. Stellar & Planetary Properties

The stellar parameters of our final selected sample (taken from the TESS input catalog; Stassun et al. 2018) are listed in Table 1. In the main our target stars are roughly Sun-like FGK dwarfs, with only two stars hotter than 6000 K and only two cooler than 4000 K. The stars are moderately bright; the brightest, TOI-6054 (HD 23074), has $m_V = 8.0$ mag but the rest of the sample has a median brightness of $m_V = 10.4$ mag and $m_J = 9.0$ mag (suitable for JWST spectroscopy with most time-series modes). Stellar activity levels, photometric variability, and rotation periods are not known for all our stars but characterizing these properties is a key goal of Theme II (Sec. 2.4).

Our resulting planet sample spans a wide range of sub-Neptune parameter space. The sample has a median radius of $2.5R_\oplus$ with six planets larger than $3R_\oplus$, and Fig. 4 shows that the planets mostly lie above the radius gap (Fulton & Petigura 2018). Thus the majority of our targets are likely to be volatile-dominated water worlds or mini-Neptunes (Lopez & Fortney 2014). Our targets have a median equilibrium temperature of 800 K, suggesting that many of them may be warm enough to inhibit aerosol production and so reveal atmospheric features in transmission (Brande et al. 2024). The planets have a median orbital period of just 8 days; this value is comfortably shorter than the typical rotation periods of mature Sun-like stars, which will (we hope) result in relatively straightforward RV analyses. Finally, our sub-Neptune targets have a median estimated TSM of 56, indicating good prospects for atmospheric charac-

terization via transmission spectroscopy. In particular, TOI-5799.01 has an estimated TSM of 114, marking it as potentially the best atmospheric target in our sample. Nonetheless, given the broad diversity of sub-Neptune compositions we expect our targets' TSM values will change significantly from these estimated values once the planets' masses are measured.

5.2. Observing Strategy

Since February 2024, OrCAS RVs are being observed with Keck/KPF through a multi-semester NASA KSMS award and on a semester-to-semester basis with WIYN/NEID awards through UW-Madison and NOIR-Lab. Though both instruments are both designed to achieve comparable levels of RV precision, NEID is necessarily limited to somewhat brighter stars given WIYN's moderate (3.5 m) aperture diameter. We are therefore using NEID to observe our brightest stellar targets (TOI-6054/HD 23074, TOI-1799/HD 96735, and TOI-1247/HD 135694; see Table 1) while focusing KPF on the fainter systems.

We aim to observe all targets 1-2 times per semester with KPF to provide sensitivity to longer-period, massive companions, and intensively (up to ~ 30 times) within a single observing season to densely sample both the target planet's Doppler signal as well as other RV signals (such as those arising from stellar activity). To the extent possible, we attempt to adopt a similar approach with our NEID targets. Integration times are set to achieve an internal, instrumental Doppler precision of 0.5 m s^{-1} ; for KPF this corresponds to roughly 4–20 minutes (depending on m_V and $v \sin i$).

We aim to schedule each target's RV observations to have approximately uniform orbital phase coverage. This approach results in the least biased, and most significant, set of final mass measurements (Burt et al. 2018; Cabona et al. 2021). For the queue-based WIYN/NEID such scheduling is relatively simple to achieve; however classically-scheduled observations with Keck/KPF will somewhat affect our ability to achieve an optimal observing cadence with roughly uniform phase coverage.

6. CONCLUSION

The best hope for characterizing sub-Neptunes (the most common planets in our Milky Way) is to undertake Doppler spectroscopy (RV) mass measurements, followed by atmospheric characterization, of planet candidates orbiting nearby stars. In particular, a precisely measured mass is essential to interpret transmission spectroscopy of transiting sub-Neptunes. By providing a large sample of such masses, RV programs keep the target pipeline flowing for JWST (and ARIEL) and ensure

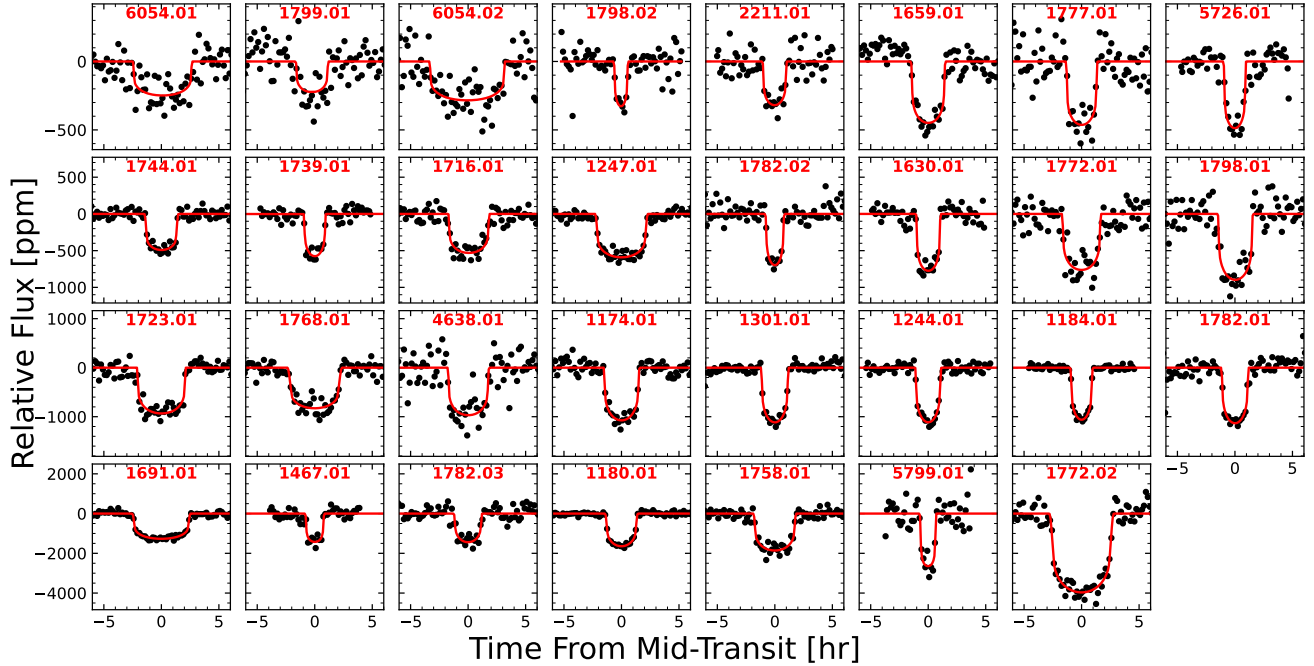


Figure 3. Transit light-curve fits to our target sample, showing *TESS* photometry (black points, binned to a 10-minute cadence) and the best-fit light curves (red line).

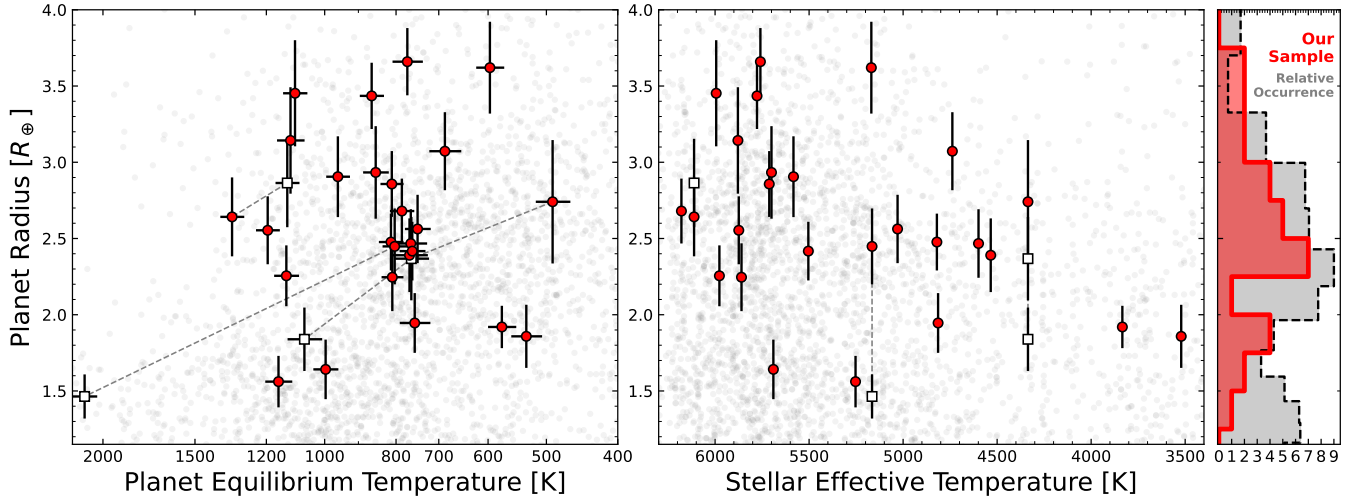


Figure 4. Our target sample, showing the distribution of fit planet size, temperature, and stellar T_{eff} . Red points are our primary sample, white points are known companions to our targets, dashed lines connect planets orbiting the same target star, and light gray points are other known exoplanets. The histogram at *right* shows how our planet sizes (red) compare to the intrinsic occurrence of sub-Neptunes (gray, [Fulton & Petigura 2018](#)). Noted that these best-fit radii differ from the *TESS*-reported radii plotted in [Fig. 2c](#).

that those missions need not ‘gamble’ by observing targets with unknown or only poorly-constrained masses.

Today there are over 500 sub-Neptune TOIs (planet candidates) suitable for atmospheric characterization but lacking precise (i.e., 5σ) masses. Since 2018 the *TESS* follow-up community has measured roughly 25 planet masses (or upper limits) per year. With coordina-

tion and sufficient telescope time allocation, the community should be able to measure the masses of all 500 sub-Neptune atmospheric targets within the next 20 years. The OrCAS program is an integral part of this effort.

For these reasons we have thus designed the OrCAS survey, whose overall goals, target selection metric, and observing strategy are presented in this paper. Our two-

year mission: to seek out newly-identified, sub-Neptune-sized *TESS* planet candidates suitable for atmospheric characterization via transmission spectroscopy and then measure their masses using precise Doppler (RV) spectroscopy. We have therefore identified a sample of 26 sub-Neptune transit signals that are well-validated, are unlikely to be false positives, that present good prospects for atmospheric characterization, and whose masses can be measured with a reasonable investment of observing time. Our first mass measurements, for the two sub-Neptunes in the TOI-6054/HD 23074 system using WIYN/NEID radial velocities (Kroft et al., in prep.) are an early validation of our survey strategy. Alongside this paper, we also present Python code to directly calculate our prioritization metric for any given planet candidate; this should ultimately allow target selection biases to be minimized in any subsequent analysis of planetary mass-radius relations.

OrCAS will therefore identify high-priority targets for atmospheric spectroscopy by measuring precise masses of new planet candidates (Science Theme I). Along the way we hope to also constrain interior compositions of planets straddling the super-Earth/sub-Neptune boundary (Theme II), measure system architectures (Theme III), and quantify stellar activity in planet-hosting systems across a range of stellar types (Theme IV). We hope that the survey will also be useful for addressing additional ancillary science cases; e.g., comparing stellar abundance patterns to the abundances of the stars' hosted planets (Polanski et al. 2022; Kolecki & Wang 2022; Hejazi et al. 2023). In this way our survey will contribute to advancing our understanding of the origin, compositions, and atmospheres of sub-Neptune exoplanets.

We thank Dr. S. Halverson for advice on the performance of both NEID and KPF, and our anonymous referee for comments that improved the quality of the final manuscript.

This research was selected under the Keck Strategic Mission Support (KSMS) category of NASA's Keck General Observing program which is managed by the NASA Exoplanet Science Institute (NExSci) and funded under the auspices of NASA's Astrophysics Data Analysis Program (NASA Award Number). Data presented herein were obtained at the W. M. Keck Observatory from telescope time allocated to the National Aeronautics and Space Administration through the agency's scientific partnership with the California Institute of Technology and the University of California. NASA's time on the Keck telescopes is administered by the NASA Exoplanet Science Institute. The Observatory was made

possible by the generous financial support of the W. M. Keck Foundation.

Funding for the *TESS* mission is provided by NASA's Science Mission directorate. We acknowledge the use of public *TESS* Alert data from pipelines at the *TESS* Science Office and at the *TESS* Science Processing Operations Center. This research has made use of the Exoplanet Follow-up Observation Program website, which is operated by the California Institute of Technology, under contract with the National Aeronautics and Space Administration under the Exoplanet Exploration Program. This paper includes data collected by the *TESS* mission, which are publicly available from the Mikulski Archive for Space Telescopes (MAST). OrCAS is supported in part by a NASA/Keck grant 80NSSC24K1096.

The authors wish to recognize and acknowledge the very significant cultural role and reverence that the summit of Mauna Kea has always had within the indigenous Hawaiian community. We are most fortunate to have the opportunity to conduct observations from this mountain.

IJMC acknowledges support from NASA ROSES grant 24-XRP24_2-0084 , and from NASA Keck grant 80NSSC24K1096.

This work makes use of observations from the LCOGT network. Part of the LCOGT telescope time was granted by NOIRLab through the Mid-Scale Innovations Program (MSIP). MSIP is funded by NSF.

This research has made use of the Exoplanet Follow-up Observation Program (ExoFOP; DOI: 10.26134/ExoFOP5) website, which is operated by the California Institute of Technology, under contract with the National Aeronautics and Space Administration under the Exoplanet Exploration Program.

Funding for the *TESS* mission is provided by NASA's Science Mission Directorate. KAC and CNW acknowledge support from the *TESS* mission via subaward s3449 from MIT.

This paper is based on observations made with the MuSCAT3 instrument, developed by the Astrobiology Center and under financial supports by JSPS KAKENHI (JP18H05439) and JST PRESTO (JP-MJPR1775), at Faulkes Telescope North on Maui, HI, operated by the Las Cumbres Observatory.

This paper makes use of observations made with the MuSCAT2 instrument, developed by the Astrobiology Center, at TCS operated on the island of Tenerife by the IAC in the Spanish Observatorio del Teide.

Some of the observations in the paper made use of the NN-EXPLORE Exoplanet and Stellar Speckle Imager (NESSI). NESSI was funded by the NASA Exoplanet Exploration Program and the NASA Ames Re-

Table 2. Transit Light Curve Parameters:

TOI	P	T_0	T_{14}	R_P/R_*	a	R_P	S_{inc}	FPP ^a	NFPP ^a	Disposition ^b
—	[d]	[BJD _{TDB} - 2454833]	[hr]	[%]	[au]	[R_\oplus]	[S_\oplus]	—	—	—
1174.01	8.9534877 ^{+0.0000090} _{-0.000103}	4824.03302 ^{+0.00073} _{-0.00080}	3.063 ^{+0.056} _{-0.049}	3.056 ^{+0.249} _{-0.094}	0.0799 ^{+0.0030} _{-0.0033}	2.56 ^{+0.25} _{-0.20}	52.0 ^{+9.0} _{-7.8}	0.0012±0.0004	0±0	VP
1180.01	9.6867604 ^{+0.0000067} _{-0.0000064}	5117.32735 ^{+0.00047} _{-0.00049}	2.749 ^{+0.050} _{-0.035}	3.85 ^{+0.19} _{-0.17}	0.0808 ^{+0.0032} _{-0.0035}	3.07 ^{+0.27} _{-0.24}	37.0 ^{+8.1} _{-6.7}	0.0035±0.0032	0±0	VP
1184.01	5.7484338 ^{+0.0000026} _{-0.0000027}	5127.51150 ^{+0.00035} _{-0.00035}	1.888 ^{+0.033} _{-0.031}	3.18 ^{+0.14} _{-0.17}	0.0560 ^{+0.0022} _{-0.0023}	2.39 ^{+0.25} _{-0.23}	57 ⁺¹⁴ ₋₁₁	0.0001±0.0001	0±0	VP
1244.01	6.4003165 ^{+0.0000059} _{-0.0000059}	5080.80830 ^{+0.00073} _{-0.00070}	2.210 ^{+0.048} _{-0.031}	3.11 ^{+0.23} _{-0.11}	0.0607 ^{+0.0022} _{-0.0024}	2.47 ^{+0.24} _{-0.21}	56 ⁺¹² ₋₁₀	0±0	0±0	VP
1247.01	15.923476 ^{+0.000020} _{-0.000020}	5001.13926 ^{+0.00088} _{-0.00086}	4.490 ^{+0.126} _{-0.074}	2.43 ^{+0.14} _{-0.16}	0.1247 ^{+0.0048} _{-0.0052}	2.86 ^{+0.23} _{-0.21}	71.8 ^{+11.2} _{-9.6}	0.0046±0.0133	0±0	VP
1301.01	6.0964072 ^{+0.0000036} _{-0.0000036}	4877.29440 ^{+0.00033} _{-0.00034}	2.333 ^{+0.026} _{-0.021}	3.080 ^{+0.139} _{-0.067}	0.0599 ^{+0.0022} _{-0.0024}	2.48 ^{+0.20} _{-0.18}	72 ⁺¹¹ ₋₁₀	0±0	0±0	VP
1467.01	5.9711471 ^{+0.0000087} _{-0.0000085}	3933.9885 ^{+0.00013} _{-0.00013}	1.578 ^{+0.063} _{-0.044}	3.58 ^{+0.39} _{-0.18}	0.05075 ^{+0.00178} _{-0.00070}	1.92 ^{+0.17} _{-0.11}	18.1 ^{+3.4} _{-3.0}	0.0001±0	0.0001±0	VP
1630.01	12.055735 ^{+0.000015} _{-0.000015}	5098.22472 ^{+0.00091} _{-0.00110}	2.087 ^{+0.058} _{-0.036}	2.65 ^{+0.23} _{-0.11}	0.1012 ^{+0.0043} _{-0.0046}	2.42 ^{+0.23} _{-0.16}	55.6 ^{+9.8} _{-8.3}	0.0043±0.0015	0.0039±0.0014	LP
1659.01	5.877556 ^{+0.000015} _{-0.000018}	4924.3568 ^{+0.0012} _{-0.0014}	2.891 ^{+0.059} _{-0.066}	2.036 ^{+0.229} _{-0.086}	0.0658 ^{+0.0027} _{-0.0029}	2.26 ^{+0.25} _{-0.16}	268 ⁺⁴⁵ ₋₃₈	0.0056±0.0011	0±0	VP
1691.01	16.736889 ^{+0.000018} _{-0.000018}	5089.72550 ^{+0.00073} _{-0.00071}	4.980 ^{+0.054} _{-0.041}	3.335 ^{+0.129} _{-0.067}	0.1294 ^{+0.0057} _{-0.0063}	3.66 ^{+0.24} _{-0.21}	59 ⁺¹² ₋₁₀	0.0001±0.0003	0±0	VP
1716.01	8.082377 ^{+0.000028} _{-0.000027}	5126.2213 ^{+0.00026} _{-0.00025}	3.563 ^{+0.168} _{-0.100}	2.32 ^{+0.26} _{-0.18}	0.0805 ^{+0.0033} _{-0.0036}	3.14 ^{+0.41} _{-0.30}	254 ⁺⁴⁷ ₋₄₀	0.0018±0.0002	0.001±0.0001	LP
1723.01	13.727013 ^{+0.000015} _{-0.000013}	4760.95996 ^{+0.00071} _{-0.00071}	4.233 ^{+0.065} _{-0.042}	2.869 ^{+0.166} _{-0.073}	0.1135 ^{+0.0045} _{-0.0049}	3.44 ^{+0.30} _{-0.19}	92 ⁺¹⁵ ₋₁₂	0.0006±0.0001	0±0	VP
1739.01	8.3033414 ^{+0.0000092} _{-0.0000101}	4798.82035 ^{+0.00059} _{-0.00074}	1.871 ^{+0.047} _{-0.031}	2.26 ^{+0.23} _{-0.10}	0.0739 ^{+0.0029} _{-0.0031}	1.95 ^{+0.23} _{-0.17}	53.9 ^{+11.2} _{-9.5}	0.0049±0.0009	0±0	VP
1744.01	22.341703 ^{+0.000044} _{-0.000042}	5075.38440 ^{+0.00093} _{-0.00083}	2.783 ^{+0.065} _{-0.045}	2.141 ^{+0.196} _{-0.090}	0.1641 ^{+0.0073} _{-0.0080}	2.68 ^{+0.26} _{-0.17}	63.3 ^{+10.5} _{-8.9}	0.0085±0.0024	0.0068±0.0021	LP
1758.01	20.705075 ^{+0.000037} _{-0.000034}	5091.7718 ^{+0.0013} _{-0.0013}	3.673 ^{+0.080} _{-0.055}	4.06 ^{+0.29} _{-0.14}	0.1414 ^{+0.0054} _{-0.0059}	3.62 ^{+0.34} _{-0.27}	21.1 ^{+4.0} _{-3.4}	0.0002±0.0002	0±0	VP
1768.01	7.337704 ^{+0.000021} _{-0.000022}	4794.0224 ^{+0.00016} _{-0.0018}	4.56 ^{+0.13} _{-0.11}	2.87 ^{+0.31} _{-0.21}	0.0764 ^{+0.0033} _{-0.0036}	3.45 ^{+0.42} _{-0.29}	240 ⁺³⁹ ₋₃₃	0.0076±0.0035	0.0032±0.0007	LP
1772.01	8.054247 ^{+0.000040} _{-0.000038}	4795.8507 ^{+0.00028} _{-0.0026}	3.42 ^{+0.13} _{-0.10}	2.66 ^{+0.30} _{-0.14}	0.0784 ^{+0.0032} _{-0.0035}	2.91 ^{+0.33} _{-0.21}	140 ⁺²² ₋₁₉	0.0002±0.0001	0.0001±0	VP
1772.02	30 ^e	4785.70772 ^{+0.00097} _{-0.00094}	5.506 ^{+0.109} _{-0.073}	5.90 ^{+0.25} _{-0.13}	—	6.44 ^{+0.41} _{-0.34}	—	—	—	STPC
1777.01	14.650112 ^{+0.000082} _{-0.000080}	4802.1067 ^{+0.0029} _{-0.0031}	2.64 ^{+0.13} _{-0.12}	2.09 ^{+0.25} _{-0.13}	0.1195 ^{+0.0048} _{-0.0052}	2.25 ^{+0.28} _{-0.18}	71.3 ^{+10.6} _{-9.0}	0.067±0.0056	0.0005±0.0001	LP
1782.01 ^c	4.9876410 ^{+0.0000092} _{-0.0000098}	4802.7331 ^{+0.0011} _{-0.0010}	2.328 ^{+0.078} _{-0.050}	3.21 ^{+0.34} _{-0.17}	0.0502 ^{+0.0018} _{-0.0020}	2.37 ^{+0.31} _{-0.24}	56 ⁺¹³ ₋₁₁	0.0028±0.0009	0±0	VP
1782.02 ^c	1.8290242 ^{+0.0000023} _{-0.0000020}	4799.81673 ^{+0.00056} _{-0.00061}	1.544 ^{+0.030} _{-0.031}	2.49 ^{+0.25} _{-0.12}	0.02574 ^{+0.00094} _{-0.00101}	1.84 ^{+0.23} _{-0.19}	214 ⁺⁵⁰ ₋₄₂	0.0020±0.0002	0±0	VP
1782.03	18.75569 ^{+0.00012} _{-0.00013}	4792.0534 ^{+0.00026} _{-0.0033}	2.53 ^{+0.26} _{-0.16}	3.72 ^{+0.61} _{-0.33}	0.1215 ^{+0.0044} _{-0.0048}	2.74 ^{+0.48} _{-0.34}	9.6 ^{+2.3} _{-1.9}	0.027±0.0041	0±0	LP
1798.01	8.021522 ^{+0.000024} _{-0.000028}	4855.1359 ^{+0.00021} _{-0.00031}	3.13 ^{+0.17} _{-0.11}	2.85 ^{+0.36} _{-0.15}	0.0750 ^{+0.0030} _{-0.0032}	2.45 ^{+0.32} _{-0.19}	69.3 ^{+11.6} _{-9.9}	0.0003±0.0001	0±0	VP
1798.02 ^c	0.43781182 ^{+0.0000053} _{-0.0000061}	4858.31350 ^{+0.00071} _{-0.00082}	1.215 ^{+0.051} _{-0.111}	1.706 ^{+0.209} _{-0.087}	0.01079 ^{+0.00043} _{-0.00046}	1.46 ^{+0.18} _{-0.11}	3345 ⁺⁵⁵⁹ ₋₄₇₈	0.716±0.014	0.0178±0.0007	VP ^d
1799.01	7.0946 ^{+0.0032} _{-0.0023}	4071.8176 ^{+0.0060} _{-0.0047}	2.57 ^{+0.26} _{-0.17}	1.57 ^{+0.20} _{-0.14}	0.0725 ^{+0.0030} _{-0.0033}	1.64 ^{+0.23} _{-0.17}	164 ⁺²⁷ ₋₂₃	0.001±0.0001	0±0	VP
2211.01	3.092687 ^{+0.000013} _{-0.000012}	4205.1032 ^{+0.0027} _{-0.0024}	2.06 ^{+0.12} _{-0.11}	1.71 ^{+0.20} _{-0.12}	0.0401 ^{+0.0016} _{-0.0017}	1.56 ^{+0.20} _{-0.14}	296 ⁺⁵⁴ ₋₄₆	0.0087±0.0003	0.0031±0.0001	LP
4638.01	10.283919 ^{+0.000093} _{-0.000099}	4616.3508 ^{+0.00039} _{-0.0032}	3.72 ^{+0.21} _{-0.18}	2.99 ^{+0.37} _{-0.19}	0.0930 ^{+0.0038} _{-0.0042}	2.93 ^{+0.38} _{-0.24}	87 ⁺¹⁵ ₋₁₂	0.0035±0.0004	0.0002±0	VP
5726.01	5.4911252 ^{+0.000095} _{-0.000146}	4010.5951 ^{+0.00023} _{-0.0012}	1.887 ^{+0.048} _{-0.036}	2.101 ^{+0.219} _{-0.095}	0.0622 ^{+0.0025} _{-0.0027}	2.55 ^{+0.28} _{-0.18}	338 ⁺⁵⁴ ₋₄₆	0.0084±0.0013	0.0002±0	VP
5799.01	4.16466 ^{+0.00060} _{-0.00063}	4939.3345 ^{+0.0020} _{-0.0020}	1.51 ^{+0.15} _{-0.11}	4.96 ^{+0.66} _{-0.42}	0.03490 ^{+0.00070} _{-0.00073}	1.86 ^{+0.26} _{-0.17}	13.4 ^{+2.8} _{-2.4}	0.0001±0	0.0001±0	VP
6054.01	7.4930 ^{+0.0059} _{-0.0055}	5080.1303 ^{+0.0084} _{-0.0091}	5.56 ^{+0.41} _{-0.29}	1.496 ^{+0.177} _{-0.092}	0.0785 ^{+0.0034} _{-0.0038}	2.64 ^{+0.32} _{-0.21}	529 ⁺⁸⁶ ₋₇₂	0.0054±0.0031	0±0	VP
6054.02 ^c	12.5750 ^{+0.0070} _{-0.0072}	5086.9199 ^{+0.0065} _{-0.0059}	6.56 ^{+0.26} _{-0.25}	1.622 ^{+0.202} _{-0.100}	0.1109 ^{+0.0049} _{-0.0053}	2.86 ^{+0.37} _{-0.23}	265 ⁺⁴³ ₋₃₆	0±0	0±0	VP

^a FPP and NFPP values < 10⁻⁴ are reported here as zero.^b Statistical validation disposition following Giacalone et al. (2021): VP (Validated Planet), LP (Likely Planet), or STPC (single-transit planet candidate).^c Target names in italics are companions of our selected targets, but were not themselves selected by our prioritization metric.^d Planet confirmed via RV mass measurement of 5.6^{+0.8}_{-0.7} M_⊕ (Polanski et al. 2024).^e Single-transit planet candidate; period set to 30 d for transit fit.

search Center. NESSI was built at the Ames Research Center by Steve B. Howell, Nic Scott, Elliott P. Horch, and Emmett Quigley.

This research was carried out at the Jet Propulsion Laboratory, California Institute of Technology, under a contract with the National Aeronautics and Space Administration (80NM0018D0004).

We thank TÜBİTAK for a partial support in using T100 telescope with project number 23BT100-2045.

The postdoctoral fellowship of KB is funded by F.R.S.-FNRS grant T.0109.20 and by the Francqui Foundation.

This work is partly supported by JSPS KAKENHI Grant Number JP24H00017, JP24K00689, and JSPS Bilateral Program Number JPJSBP120249910.

Some of the observations in this paper made use of the High-Resolution Imaging instrument ‘Alopeke and were obtained under Gemini LLP Proposal Number: GN/S-2021A-LP-105. ‘Alopeke was funded by the NASA Exoplanet Exploration Program and built at the NASA Ames Research Center by Steve B. Howell, Nic Scott, Elliott P. Horch, and Emmett Quigley. Alopeke was mounted on the Gemini North telescope of the international Gemini Observatory, a program of NSF’s OIR Lab, which is managed by the Association of Universities for Research in Astronomy (AURA) under a cooperative

agreement with the National Science Foundation. on behalf of the Gemini partnership: the National Science Foundation (United States), National Research Council (Canada), Agencia Nacional de Investigacion y Desarrollo (Chile), Ministerio de Ciencia, Tecnología e Innovacion (Argentina), Ministerio da Ciencia, Tecnologia, Inovacoes e Comunicacoes (Brazil), and Korea Astronomy and Space Science Institute (Republic of Korea).

Support for this work was provided by NASA through the NASA Hubble Fellowship grant HST-HF2-51559.001-A awarded by the Space Telescope Science Institute, which is operated by the Association of Universities for Research in Astronomy, Inc., for NASA, under contract NAS5-26555.

T.D. acknowledges support from the McDonnell Center for the Space Sciences at Washington University in St. Louis.

Facilities: TESS, Keck:I (KPF), WIYN (NEID), LCOGT, WIYN (NESSI), Gemini (NIRI), Gemini (‘Alopeke), Palomar (PHARO), Keck:II (NIRC2)

Software: `emcee` (Foreman-Mackey et al. 2013), `BATMAN` (Kreidberg 2015), `LDTK` (Parviainen & Aigrain 2015), `Lightkurve` (Lightkurve Collaboration et al. 2018), `SciPy` (Virtanen et al. 2020), `matplotlib` (Barrett et al. 2005), `AstroImageJ` (Collins et al. 2017), `TAPIR` (Jensen 2013)

REFERENCES

- Adams, E. R., Seager, S., & Elkins-Tanton, L. 2008, *ApJ*, 673, 1160
- Aigrain, S., Pont, F., & Zucker, S. 2012, *MNRAS*, 419, 3147
- Akana Murphy, J. M., Luque, R., & Batalha, N. M. 2024, arXiv e-prints, arXiv:2411.02521
- Alderson, L., Batalha, N. E., Wakeford, H. R., et al. 2024, *AJ*, 167, 216
- Armstrong, D. J., Lopez, T. A., Adibekyan, V., et al. 2020, *Nature*, 583, 39
- Barrett, P., Hunter, J., Miller, J. T., Hsu, J. C., & Greenfield, P. 2005, in *Astronomical Society of the Pacific Conference Series*, Vol. 347, *Astronomical Data Analysis Software and Systems XIV*, ed. P. Shopbell, M. Britton, & R. Ebert, 91
- Bastien, F. A., Stassun, K. G., Basri, G., & Pepper, J. 2013, *Nature*, 500, 427
- Batalha, N. E., Lewis, T., Fortney, J. J., et al. 2019, *ApJL*, 885, L25
- Beard, C., Robertson, P., Giovinazzi, M. R., et al. 2024, arXiv e-prints, arXiv:2408.02873
- Beatty, T. G., Welbanks, L., Schlawin, E., et al. 2024, *ApJL*, 970, L10
- Bell, T. J., Welbanks, L., Schlawin, E., et al. 2023, arXiv e-prints, arXiv:2309.04042
- Bitsch, B., & Izidoro, A. 2023, *A&A*, 674, A178
- Bonomo, A. S., Dumusque, X., Massa, A., et al. 2023, *A&A*, 677, A33
- Borucki, W. J., Koch, D. G., Batalha, N., et al. 2012, *ApJ*, 745, 120
- Bourrier, V., Lovis, C., Cretignier, M., et al. 2021, *A&A*, 654, A152
- Bowler, B. P. 2016, *PASP*, 128, 102001
- Brande, J., Crossfield, I. J. M., Kreidberg, L., et al. 2024, *ApJL*, 961, L23
- Brown, T. M., Baliber, N., Bianco, F. B., et al. 2013, *Publications of the Astronomical Society of the Pacific*, 125, 1031
- Burt, J., Holden, B., Wolfgang, A., & Bouma, L. G. 2018, *AJ*, 156, 255
- Cabona, L., Viana, P. T. P., Landoni, M., & Faria, J. P. 2021, *MNRAS*, 503, 5504
- Cale, B. L., Reefer, M., Plavchan, P., et al. 2021, *AJ*, 162, 295

- Chontos, A., Murphy, J. M. A., MacDougall, M. G., et al. 2022, *AJ*, 163, 297
- Cloutier, R., Astudillo-Defru, N., Doyon, R., et al. 2019, *A&A*, 621, A49
- Collins, K. 2019, in *American Astronomical Society Meeting Abstracts*, Vol. 233, *American Astronomical Society Meeting Abstracts #233*, 140.05
- Collins, K. A., Kielkopf, J. F., Stassun, K. G., & Hessman, F. V. 2017, *AJ*, 153, 77
- Crass, J., Gaudi, B. S., Leifer, S., et al. 2021, arXiv e-prints, arXiv:2107.14291
- Cretignier, M., Dumusque, X., Aigrain, S., & Pepe, F. 2023, arXiv e-prints, arXiv:2308.11812
- Crossfield, I. J. M. 2023, *ApJL*, 952, L18
- Crossfield, I. J. M., Petigura, E., Schlieder, J. E., et al. 2015, *ApJ*, 804, 10
- Crossfield, I. J. M., Ciardi, D. R., Petigura, E. A., et al. 2016, *ApJS*, 226, 7
- Dekany, R., Roberts, J., Burruss, R., et al. 2013, *ApJ*, 776, 130
- Deming, L. D., & Seager, S. 2017, *Journal of Geophysical Research (Planets)*, 122, 53
- Figueira, P., Pont, F., Mordasini, C., et al. 2009, *A&A*, 493, 671
- Foreman-Mackey, D., Hogg, D. W., Lang, D., & Goodman, J. 2013, *PASP*, 125, 306
- Fukui, A., Narita, N., Tristram, P. J., et al. 2011, *PASJ*, 63, 287
- Fulton, B. J., & Petigura, E. A. 2018, *AJ*, 156, 264
- Fulton, B. J., Petigura, E. A., Howard, A. W., et al. 2017, *AJ*, 154, 109
- Furlan, E., Ciardi, D. R., Everett, M. E., et al. 2017, *AJ*, 153, 71
- Galland, F., Lagrange, A.-M., Udry, S., et al. 2005, *A&A*, 443, 337
- Gavel, D., Kupke, R., Dillon, D., et al. 2014, in *Society of Photo-Optical Instrumentation Engineers (SPIE) Conference Series*, Vol. 9148, *Adaptive Optics Systems IV*, ed. E. Marchetti, L. M. Close, & J.-P. Vran, 914805
- Giacalone, S., Dressing, C. D., Jensen, E. L. N., et al. 2021, *AJ*, 161, 24
- Gibson, S. R., Howard, A. W., Marcy, G. W., et al. 2016, in *Society of Photo-Optical Instrumentation Engineers (SPIE) Conference Series*, Vol. 9908, *Ground-based and Airborne Instrumentation for Astronomy VI*, ed. C. J. Evans, L. Simard, & H. Takami, 990870
- Gilbert, G., & Petigura, E. 2024, in *AAS/Division for Extreme Solar Systems Abstracts*, Vol. 56, *AAS/Division for Extreme Solar Systems Abstracts*, 301.05
- Hayward, T. L., Brandl, B., Pirger, B., et al. 2001, *PASP*, 113, 105
- Hejazi, N., Crossfield, I. J. M., Nordlander, T., et al. 2023, *ApJ*, 949, 79
- Hodapp, K.-W., Irwin, E. M., Yamada, H., et al. 2003, in *Proc. SPIE*, Vol. 4841, *Instrument Design and Performance for Optical/Infrared Ground-based Telescopes*, ed. M. Iye & A. F. M. Moorwood, 869–880
- Howard, A. W., Marcy, G. W., Johnson, J. A., et al. 2010, *Science*, 330, 653
- Howell, S. B., Everett, M. E., Sherry, W., Horch, E., & Ciardi, D. R. 2011, *AJ*, 142, 19
- Jenkins, J. M., Twicken, J. D., McCauliff, S., et al. 2016, in *Society of Photo-Optical Instrumentation Engineers (SPIE) Conference Series*, Vol. 9913, *Software and Cyberinfrastructure for Astronomy IV*, 99133E
- Jensen, E. 2013, *Tapir: A web interface for transit/eclipse observability*, *Astrophysics Source Code Library*, ascl:1306.007
- Johnson, J. A., Petigura, E. A., Fulton, B. J., et al. 2017, *AJ*, 154, 108
- JTEC Team, Ahrer, E.-M., Alderson, L., et al. 2023, *Nature*, 614, 649
- Kanodia, S., He, M. Y., Ford, E. B., Ghosh, S. K., & Wolfgang, A. 2023, *ApJ*, 956, 76
- Kanodia, S., Wolfgang, A., Stefansson, G. K., Ning, B., & Mahadevan, S. 2019, *ApJ*, 882, 38
- Kempton, E. M. R., Bean, J. L., Louie, D. R., et al. 2018, *PASP*, 130, 114401
- Kolecki, J. R., & Wang, J. 2022, *AJ*, 164, 87
- Konopacky, Q. M., Barman, T. S., Macintosh, B. A., & Marois, C. 2013, *Science*, 339, 1398
- Kreidberg, L. 2015, *PASP*, 127, 1161
- Kupke, R., Gavel, D., Roskosi, C., et al. 2012, in *Society of Photo-Optical Instrumentation Engineers (SPIE) Conference Series*, Vol. 8447, *Adaptive Optics Systems III*, ed. B. L. Ellerbroek, E. Marchetti, & J.-P. Véran, 84473G
- Libby-Roberts, J. E., Berta-Thompson, Z. K., Désert, J.-M., et al. 2020, *AJ*, 159, 57
- Lightkurve Collaboration, Cardoso, J. V. d. M., Hedges, C., et al. 2018, *Lightkurve: Kepler and TESS time series analysis in Python*, *Astrophysics Source Code Library*, record ascl:1812.013, ascl:1812.013
- Lissauer, J. J., Ragozzine, D., Fabrycky, D. C., et al. 2011, *ApJS*, 197, 8
- Lopez, E. D., & Fortney, J. J. 2014, *ApJ*, 792, 1
- Lothringer, J. D., Rustamkulov, Z., Sing, D. K., et al. 2021, *ApJ*, 914, 12
- Luhn, J. K., Ford, E. B., Guo, Z., et al. 2023, *AJ*, 165, 98

- Luque, R., & Pallé, E. 2022, *Science*, 377, 1211
- Madhusudhan, N., Sarkar, S., Constantinou, S., et al. 2023, arXiv e-prints, arXiv:2309.05566
- Mamajek, E., & Stapelfeldt, K. 2024, arXiv e-prints, arXiv:2402.12414
- McCully, C., Volgenau, N. H., Harbeck, D.-R., et al. 2018, in *Society of Photo-Optical Instrumentation Engineers (SPIE) Conference Series*, Vol. 10707, Proc. SPIE, 107070K
- McGurk, R., Rockosi, C., Gavel, D., et al. 2014, in *Society of Photo-Optical Instrumentation Engineers (SPIE) Conference Series*, Vol. 9148, Adaptive Optics Systems IV, ed. E. Marchetti, L. M. Close, & J.-P. Vran, 91483A
- Millholland, S. C., He, M. Y., & Zink, J. K. 2022, *AJ*, 164, 72
- Naponiello, L., Mancini, L., Sozzetti, A., et al. 2023, arXiv e-prints, arXiv:2309.01464
- Narita, N., Fukui, A., Kusakabe, N., et al. 2015, *Journal of Astronomical Telescopes, Instruments, and Systems*, 1, 045001
- Narita, N., Fukui, A., Kusakabe, N., et al. 2019, *J. Astron. Telesc. Instruments, Syst.*, 5, 015001
- Narita, N., Fukui, A., Yamamuro, T., et al. 2020, in *Society of Photo-Optical Instrumentation Engineers (SPIE) Conference Series*, Vol. 11447, Society of Photo-Optical Instrumentation Engineers (SPIE) Conference Series, 114475K
- Ning, B., Wolfgang, A., & Ghosh, S. 2018, *ApJ*, 869, 5
- Otegi, J. F., Bouchy, F., & Helled, R. 2020, *A&A*, 634, A43
- Ould-Elhkim, M., Moutou, C., Donati, J. F., et al. 2023, *A&A*, 675, A187
- Owen, J. E. 2019, *Annual Review of Earth and Planetary Sciences*, 47, 67
- Parc, L., Bouchy, F., Venturini, J., Dorn, C., & Helled, R. 2024, *A&A*, 688, A59
- Parviainen, H., & Aigrain, S. 2015, *MNRAS*, 453, 3821
- Parviainen, H., Luque, R., & Palle, E. 2024, *MNRAS*, 527, 5693
- Parviainen, H., Tingley, B., Deeg, H. J., et al. 2019, *A&A*, 630, A89
- Petigura, E. A., Howard, A. W., Marcy, G. W., et al. 2017, *AJ*, 154, 107
- Polanski, A. S., Crossfield, I. J. M., Howard, A. W., Isaacson, H., & Rice, M. 2022, *Research Notes of the American Astronomical Society*, 6, 155
- Polanski, A. S., Lubin, J., Beard, C., et al. 2024, *ApJS*, 272, 32
- Radica, M., Artigau, É., Lafrenière, D., et al. 2022, *MNRAS*, 517, 5050
- Rogers, J. G., Schlichting, H. E., & Owen, J. E. 2023, *ApJL*, 947, L19
- Savel, A. B., Dressing, C. D., Hirsch, L. A., et al. 2020, *AJ*, 160, 287
- Savel, A. B., Hirsch, L. A., Gill, H., Dressing, C. D., & Ciardi, D. R. 2022, *PASP*, 134, 124501
- Schlieder, J. E., Gonzales, E. J., Ciardi, D. R., et al. 2021, *Frontiers in Astronomy and Space Sciences*, 8, 63
- Schwab, C., Rakich, A., Gong, Q., et al. 2016, in *Society of Photo-Optical Instrumentation Engineers (SPIE) Conference Series*, Vol. 9908, Ground-based and Airborne Instrumentation for Astronomy VI, ed. C. J. Evans, L. Simard, & H. Takami, 99087H
- Scott, N. J., & Howell, S. B. 2018, in *Society of Photo-Optical Instrumentation Engineers (SPIE) Conference Series*, Vol. 10701, Optical and Infrared Interferometry and Imaging VI, 107010G
- Sing, D. K., Rustamkulov, Z., Thorngren, D. P., et al. 2024, arXiv e-prints, arXiv:2405.11027
- Stassun, K. G., Oelkers, R. J., Pepper, J., et al. 2018, *AJ*, 156, 102
- Teske, J., Wang, S. X., Wolfgang, A., et al. 2021, *ApJS*, 256, 33
- Tinetti, G., Drossart, P., Eccleston, P., et al. 2018, *Experimental Astronomy*, 46, 135
- Tsai, S.-M., Lee, E. K. H., Powell, D., et al. 2023, *Nature*, 617, 483
- Virtanen, P., Gommers, R., Oliphant, T. E., et al. 2020, *Nature Methods*, 17, 261
- Wallack, N. L., Batalha, N. E., Alderson, L., et al. 2024, arXiv e-prints, arXiv:2404.01264
- Weiss, L. M., Marcy, G. W., Petigura, E. A., et al. 2018, *AJ*, 155, 48
- Welbanks, L., Bell, T. J., Beatty, T. G., et al. 2024, *Nature*, 630, 836
- Winn, J. N. 2010, arXiv e-prints, arXiv:1001.2010
- Winn, J. N., & Fabrycky, D. C. 2015, *ARA&A*, 53, 409
- Wizinowich, P., Acton, D. S., Shelton, C., et al. 2000, *PASP*, 112, 315
- Wolfgang, A., Rogers, L. A., & Ford, E. B. 2016, *ApJ*, 825, 19
- Yu, J., Huber, D., Bedding, T. R., & Stello, D. 2018, *MNRAS*, 480, L48
- Zechmeister, M., Reiners, A., Amado, P. J., et al. 2018, *A&A*, 609, A12

APPENDIX

A. GROUND-BASED LIGHTCURVE FOLLOW-UP

The *TESS* pixel scale is $\sim 21''$ pixel⁻¹ and photometric apertures typically extend out to roughly 1 arcminute, generally causing multiple stars to blend in the *TESS* aperture. To rule out a nearby eclipsing binary (NEB) as the potential source of a *TESS* detection and attempt to detect the signal on-target, we observed our target stars and the nearby fields as part of the *TESS* Follow-up Observing Program⁴ Sub Group 1 (TFOP; Collins 2019). In some cases, we also observed in multiple bands across the optical spectrum to check for wavelength dependent transit depth differences, which can be suggestive of a planet candidate false positive. We used the *TESS* Transit Finder, which is a customized version of the Tapir software package (Jensen 2013), to schedule our transit observations. All observations were reduced using AstroImageJ (Collins et al. 2017), except for MuSCAT and MuSCAT2 as noted in Table 4.

All of our light curve follow-up observations are summarized in Table 4 and all light curve data are available on the EXOFOP-*TESS* website⁵. We also provide a short summary of each light curve result and an overall final photometric follow-up disposition in the table. For the targets in this survey, we assign four light curve follow-up dispositions (PC, CPC, VPC, VPC+) to indicate differing levels of confidence that a *TESS* detection is on-target, as described below.

The planet candidate (PC) disposition indicates that we either have no light curve follow-up observations, or the light curve observations are unable to confirm that the *TESS*-detected event is on-target relative to Gaia DR3 and TIC version 8 stars. TOI-1716.01, TOI-1744.01, TOI-1174.01, TOI-1777.01, TOI-4638.01, TOI-5726.01, and TOI-6054.01 have a PC disposition and are not listed in Table 4.

The cleared planet candidate (CPC) disposition indicates that we have confined the *TESS*-detection to occur on the target star relative to all Gaia DR3 and TIC version 8 stars. Using ground-based photometry, we check all stars out to 2.5 from the target star that are bright enough, assuming a 100% eclipse, in *TESS*-band to produce the *TESS*-detected depth at mid-transit. To account for possible delta-magnitude differences between *TESS*-band and the follow-up band, and to account for *TESS*-band magnitude errors, we included an extra 0.5 magnitudes fainter in *TESS*-band. For these cases, the transit depth is generally too shallow to detect on-target in ground-based follow-up observations, so we often saturate the target star on the detector to enable a complete search of all necessary fainter nearby stars. Since the *TESS* point-spread-function has full-width-half-maximum of roughly 40'', and the irregularly shaped SPOC photometric apertures and circular QLP photometric apertures generally extend to $\sim 1'$ from the target star, we check for events in stars out to 2.5 from the target star. For a star to be considered “cleared” of an NEB signal, we require its light curve to have a flat model residual RMS value at least a factor of 3 smaller than the eclipse depth required to produce the *TESS* detection in the star. We ensure that the predicted ephemeris uncertainty is covered by at least $\pm 3\sigma$ relative to the most precise SPOC or QLP ephemeris available at the time of publication. Finally, we check all nearby star light curves by eye to ensure that no obvious eclipse-like event is present. By process of elimination, we conclude that when all necessary nearby stars are “cleared” of NEBs, the transit is indeed occurring on-target, or in a star so close to the target star, that it was not detected by Gaia DR3 and is not in TIC version 8.

The verified planet candidate (VPC) disposition indicates that we have confirmed using ground-based follow-up light curve photometry that the *TESS*-detected event is occurring on-target. This is accomplished using follow-up photometric apertures that are small enough to exclude most or all of the flux from the nearest Gaia DR3 and/or TIC version 8 star that is bright enough to be capable of producing the *TESS* signal.

The verified planet candidate plus (VPC+) disposition is the same as VPC, except we have measured transit depths in the target star follow-up photometric apertures across several optical bands. We elevate the disposition to VPC+ if no strong ($> 3\sigma$) transit depth difference is detected across the bands.

B. GROUND-BASED HIGH-RESOLUTION IMAGING FOLLOW-UP

Below we briefly describe our high-resolution imaging observations of these systems. These observations (summarized in Table 3) provided the imaging data used as input for the TRICERATOPS statistical validation analysis described in Sec. 3.2. In all cases, the final processed data products, stacked images, and sensitivity curves are available from at the ExoFOP website⁶.

⁴ <https://tess.mit.edu/followup/>

⁵ <https://exofop.ipac.caltech.edu/tess/>

⁶ <https://exofop.ipac.caltech.edu/>

Table 3. High-resolution imaging observations

TOI	Instrument	Observatory	PI	Date	Filter	pixel scale ["]	PSF FWHM ["]
1174	Alopeke	Gemini-N	Howell	2020-02-17	832nm	0.01	0.02
1180	NESSI	WIYN	Everett	2022-04-21	832nm	0.02	0.06
1184	NIRI	Gemini-S	Matthews	2019-11-02	Br- γ	0.022	0.113
1244	NIRC2	Keck II	Gonzales	2022-06-23	K	0.0099	0.051
1247	NIRC2	Keck II	Gonzales	2020-05-28	Br- γ	0.0099	0.052
1301	Alopeke	Gemini-N	Howell	2020-06-06	832nm	0.01	0.02
1467	NIRC2	Keck II	Gonzales	2020-09-09	K	0.0099	0.05
1630	Alopeke	Gemini-N	Howell	2021-10-17	832nm	0.01	0.02
1659	Alopeke	Gemini-N	Crossfield	2020-06-06	832nm	0.01	0.02
1691	Alopeke	Gemini-N	Crossfield	2020-06-08	832nm	0.01	0.02
1716	Alopeke	Gemini-N	Howell	2021-10-24	832nm	0.01	0.02
1723	ShARCS	Shane	Giacalone	2020-12-01	Ks	0.033	0.209
1739	Alopeke	Gemini-N	Crossfield	2020-06-08	832nm	0.01	0.02
1744	NIRC2	Keck II	Gonzales	2020-09-09	Br- γ	0.0099	0.048
1758	Alopeke	Gemini-N	Howell	2021-10-17	832nm	0.01	0.02
1768	PHARO	Hale	Ciardi	2022-02-13	Br- γ	0.025	0.099
1772	PHARO	Hale	Ciardi	2021-02-23	Br- γ	0.025	0.093
1777	PHARO	Hale	Ciardi	2020-12-04	Br- γ	0.025	0.146
1782	Alopeke	Gemini-N	Crossfield	2020-06-06	832nm	0.01	0.02
1798	Alopeke	Gemini-N	Crossfield	2020-06-06	832nm	0.01	0.02
1799	PHARO	Hale	Ciardi	2021-02-23	Br- γ	0.025	0.093
2211	Alopeke	Gemini-N	Howell	2021-06-27	832nm	0.01	0.02
4638	NESSI	WIYN	Everett	2022-09-15	832nm	0.02	0.06
5726	NESSI	WIYN	Everett	2024-02-18	832nm	0.02	0.06
5799	PHARO	Hale	Ciardi	2023-07-01	Br- γ	0.025	0.103
6054	PHARO	Hale	Ciardi	2023-11-29	Kcont	0.025	0.096

B.1. ‘Alopeke

We observed many of our target systems with the ‘Alopeke dual-channel speckle imaging instrument on Gemini-North with a pixel scale of 0.01” and a typical full width at half maximum (FWHM) resolution of 0.02”. ‘Alopeke provided simultaneous speckle imaging at 562 and 832 nm, but we used only the 832 nm data in our TRICERATOPS analysis. Typically, several sets of 1,000 short (60 ms) exposures were taken for each target, then processed with the speckle pipeline of (Howell et al. 2011).

B.2. NESSI

Three stars, TOI-1180 (UT 2022 Apr. 21), TOI-4638 (UT 2022 Sept. 15) and TOI-5726 (UT 2024 Feb. 18), were observed at the WIYN 3.5 m telescope on Kitt Peak, Arizona using the speckle imager NESSI (Scott & Howell 2018). NESSI produces simultaneous speckle images in two filters, although only the images using a filter centered at $\lambda_c = 832$ nm were used in our validation. Each observation consisted of a set of either 7 or 9 1000-frame 40 ms exposures. The field-of-view was confined using a readout region of 256×256 pixels for 4.6×4.6 arcseconds and speckle data were used to constrain the presence of additional sources out to a radius of 1.2 arcseconds from each target star. Additional observations of a single star near each science target were obtained for calibration of the underlying PSF. To reduce the data, we used the pipeline described by Howell et al. (2011). Pipeline products include a reconstructed image of the field around each target and, measured from that, a contrast curve representing the relative magnitude limit as a function of radial separation from the star. No companion sources were detected for any of the NESSI targets.

B.3. ShARCS

We observed TOI-1723 on 2020 December 2 using the ShARCS camera on the Shane 3-meter telescope at Lick Observatory (Kupke et al. 2012; Gavel et al. 2014; McGurk et al. 2014). Observations were taken with the Shane adaptive optics (AO) system in natural guide star mode in order to search for nearby, unresolved stellar companions.

We collected a single sequence of observations using a K_s filter ($\lambda_0 = 2.150 \mu\text{m}$, $\Delta\lambda = 0.320 \mu\text{m}$), achieving a contrast of 3.50 magnitudes at 0.5 arcseconds and 4.75 magnitudes at 1 arcsecond. Information about our observing strategy can be found in (Savel et al. 2020). We reduced the data using the publicly available SIMMER pipeline (Savel et al. 2022).⁷ We found no stellar companions within our detection limits. Further information about these data can be found in Dressing et al. (in prep).

B.4. PHARO

We observed several targets with high-resolution near-infrared AO imaging at Palomar Observatory with the PHARO instrument (Hayward et al. 2001) behind the P3K natural guide star system (Dekany et al. 2013). These observations were taken using a standard 5-point quincunx dither pattern with steps of $5''$ in either the narrow-band $2.1686 \mu\text{m}$ Br- γ filter or the broader Kcont filter. PHARO has a pixel scale of $0.025''$ and a total field of view of $\sim 25''$. Data were processed as described by (Furlan et al. 2017).

B.5. NIRC2

Several targets were also observed at Keck Observatory with the NIRC2 instrument (Wizinowich et al. 2000) on the 10 m Keck II telescope (see also Schlieder et al. 2021). The infrared imaging was performed in natural-guide star AO mode with short integration times designed to obtain maximum depth without saturating on the primary host star, using either the K-band filter or the narrow-band Brackett- γ filter (as an analogue for K-band for brighter stars). We used the narrow-camera mode with a pixel scale of $\sim 0.01''$, and observed in a three-point dither pattern to avoid the noisy fourth quadrant of the detector. Data were processed as described by (Furlan et al. 2017) and Schlieder et al. (2021).

B.6. NIRI

We obtained AO imaging of TOI-1184 with the Gemini Near-Infrared Imager (NIRI; Hodapp et al. 2003). We collected 9 science frames, each with an exposure time of 4.4 s, and dithered the telescope by $\sim 2''$ between each frame to use the science frames as sky background frames. The target was observed in the $2.166 \mu\text{m}$ Br- γ filter with a pixel scale of $\sim 0.022''$. Data were processed as described by (Furlan et al. 2017).

⁷ <https://github.com/arjunsavel/SIMMER>

Table 4. Ground-based light curve observations

Observatory	Ap (m)	Location	UTC Date	Filter	Result	Disp. ^a
TOI-1180.01						
GMU ^b	0.8	Fairfax, VA, USA	2019-11-10	R	no obvious NEBs in 11 NEB check stars	
Kotizarovci Obs	0.3	Viskovo, Croatia	2020-02-14	Baader R ^c	~1.7 ppt egress in 7.2'' target aperture	
Whitin Obs	0.7	Wellesley, MA, USA	2020-02-14	r'	out-of-transit coverage	
MuSCAT3 ^d -Hal	2.0	Maui, Hawai'i, USA	2022-03-11	g', r', i', z_s^e	~1.7 ppt transit in 5.3'' target apertures	
LCOGT-McD	1.0	Fort Davis, TX, USA	2022-05-18	B, z_s	~1.7 ppt transit in 5.9'' target apertures	
MuSCAT3-Hal	2.0	Maui, Hawai'i, USA	2022-04-22	g', r', i', z_s	~1.7 ppt transit in 7.2'' target apertures	VPC+
TOI-1184.01						
MuSCAT ^f -NAOJ	1.9	Okayama, Japan	2020-03-05	g', r', z_s	~1 ppt egress in 7.2'' target apertures	
MuSCAT2 ^g -TCS	1.5	Tenerife, Spain	2020-05-07	g', r', i', z_s	possible ~2 ppt 11.7'' target apertures	
LCOGT-Hal	2.0	Maui, Hawai'i, USA	2020-06-11	z_s	~1 ppt transit in 3.6'' target aperture	
LCOGT-McD	1.0	Fort Davis, TX, USA	2020-08-25	z_s	~1 ppt transit in 6.6'' target aperture	
LCOGT-Teid	1.0	Tenerife, Canary Islands	2021-08-07	i'	~1 ppt transit in 3.1'' target aperture	
LCOGT-Teid	1.0	Tenerife, Canary Islands	2022-06-22	z_s	~1 ppt transit in 4.3'' target aperture	VPC
TOI-1244.01						
GMU	0.8	Fairfax, VA, USA	2020-04-13	R	~1 ppt transit in 9.0'' target aperture	
MuSCAT3-Hal	2.0	Maui, Hawai'i, USA	2021-05-22	i'	~1 ppt transit in 4.0'' target aperture	
MuSCAT3-Hal	2.0	Maui, Hawai'i, USA	2022-07-12	g', r', i', z_s	~1 ppt ingress in 4.5'' target apertures	
MuSCAT3-Hal	2.0	Maui, Hawai'i, USA	2022-08-26	g', r', i', z_s	~1 ppt transit in 5.4'' target apertures	VPC+
TOI-1247.01						
LCOGT-McD	1.0	Fort Davis, TX, USA	2022-04-05	z_s	cleared all NEB check stars	
LCOGT-Teid	1.0	Tenerife, Canary Islands	2022-05-07	z_s	cleared 5/6 NEB check stars	CPC
TOI-1301.01						
FLWO ^h	1.2	Amado, Arizona	2021-05-22	i'	~1 ppt egress in 4.0'' target aperture	
LCOGT-Teid	1.0	Tenerife, Canary Islands	2021-09-08	i'	~1 ppt transit in 4.7'' target aperture	VPC
TOI-1467.01						
LCOGT-Teid	1.0	Tenerife, Canary Islands	2021-09-14	z_s	~1.4 ppt transit in 5.9'' target aperture	
MuSCAT3-Hal	2.0	Maui, Hawai'i, USA	2022-08-20	g', r', i', z_s	~1.4 ppt transit in 4.5'' target apertures	VPC+
TOI-1630.01						
Grand-Pra Obs	0.4	Sion Valais, Switzerland	2020-09-30	i'	cleared 35/36 NEB check stars	
LCOGT-McD	1.0	Fort Davis, TX, USA	2020-11-06	z_s	~0.8 ppt transit in 6.2'' target aperture	
LCOGT-Teid	1.0	Tenerife, Canary Islands	2021-11-14	z_s	~0.8 ppt transit in 6.6'' target aperture	VPC
TOI-1659.01						
LCOGT-Teid	1.0	Tenerife, Canary Islands	2022-10-03	z_s	cleared all NEB check stars	CPC
TOI-1691.01						
Whitin Obs	0.7	Wellesley, MA, USA	2020-02-21	r'	no obvious NEB	PC
TOI-1723.01						
LCOGT-Teid	1.0	Tenerife, Canary Islands	2022-11-26	z_s	cleared all NEBcheck stars	CPC
TOI-1739.01						
LCOGT-McD	1.0	Fort Davis, TX, USA	2022-05-15	r'	~1 ppt transit in 8.2'' target aperture	VPC
TOI-1758.01						
LCOGT-McD	1.0	Fort Davis, TX, USA	2020-11-05	B	~2 ppt transit in 4.7'' target aperture	
LCOGT-Teid	1.0	Tenerife, Canary Islands	2022-10-10	i'	~2 ppt ingress in 4.7'' target aperture	
Kotizarovci Obs	0.3	Viskovo, Croatia	2022-10-30	Baader R	~2 ppt ingress in 8.4'' target aperture	VPC
TOI-1768.01						
MuSCAT2-TCS	1.5	Tenerife, Spain	2021-01-30	g', r', i', z_s	cleared 3 of 13 NEBcheck stars	
FLWO	1.2	Amado, Arizona	2021-02-07	i'	cleared 10 of 13 NEBcheck stars	PC

Table 4 continued

Table 4 (continued)

Observatory	Ap (m)	Location	UTC Date	Filter	Result	Disp. ^a
<hr/>						
TOI-1772.01						
LCOGT-McD	1.0	Fort Davis, TX, USA	2022-12-21	z_s	cleared 5 of 5 NEBcheck stars	CPC
<hr/>						
TOI-1782.03						
FLWO	1.2	Amado, Arizona	2022-05-19	i'	~ 1.6 ppt transit in $6.2''$ target aperture	
LCOGT-McD	1.0	Fort Davis, TX, USA	2022-05-19	i'	~ 1.6 ppt transit in $6.7''$ target aperture	
LCOGT-McD	1.0	Fort Davis, TX, USA	2023-03-15	i'	~ 1.6 ppt transit in $6.2''$ target aperture	
LCOGT-McD	1.0	Fort Davis, TX, USA	2024-04-12	i'	~ 1.6 ppt ingress in $6.2''$ target aperture	VPC
<hr/>						
TOI-1798.01						
FLWO	1.2	Amado, Arizona	2021-02-09	i'	no obvious NEBs in 5 NEBcheck stars	
LCOGT-Hal	0.4	Maui, Hawai'i, USA	2021-04-06	i'	cleared 5 of 5 NEBcheck stars	CPC
<hr/>						
TOI-1799.01						
LCOGT-McD	0.4	Fort Davis, TX, USA	2021-01-02	i'	cleared 3 of 3 NEBcheck stars	CPC
<hr/>						
TOI-2211.01						
LCOGT-SSO	1.0	Coonabarabran, Australia	2021-06-15	z_s	no obvious NEBs	PC
<hr/>						
TOI-5799.01						
TRAPPIST-North	0.6	Marrakech, Morocco	2022-09-28	z'	cleared 213 of 234 NEBcheck stars	
LCOGT-Teid	1.0	Tenerife, Canary Islands	2023-06-14	i'	~ 2.6 ppt transit in $3.9''$ target aperture	
MuSCAT2-TCS	1.5	Tenerife, Spain	2023-07-08	g', r', i', z_s	~ 2.6 ppt transit in $10.8''$ target aperture	
TUG ⁱ	1.0	Antalya, Turkey	2023-08-23	g'	~ 2.6 ppt transit in $5.5''$ target aperture	VPC+

^a The overall follow-up disposition. PC = planetary candidate, CPC = cleared of NEBs, VPC = on-target relative to Gaia DR3 stars, VPC+ = achromatic on-target relative to Gaia DR3 stars. See the text for full disposition definitions.

^b George Mason University (GMU)

^c Baader R 610 nm

^d Las Cumbres Observatory Global Telescope (LCOGT; Brown et al. 2013) 0.4 m, 1.0 m, 2.0 m network nodes at Teide Observatory on the island of Tenerife (TEID), Siding Spring Observatory (SSO), McDonald Observatory (McD), and MuSCAT3 (Narita et al. 2020) on Faulkes Telescope North at Haleakala Observatory. Images calibrated by BANZAI pipeline (McCully et al. 2018) and photometry extracted using AstroImageJ (Collins et al. 2017).

^e Pan-STARRS z -short band ($\lambda_c = 8700 \text{ \AA}$, Width = 1040 \AA)

^f MuSCAT (Multicolor Simultaneous Camera for studying Atmospheres of Transiting exoplanets; Narita et al. 2015) multi-color imager is installed at the 1.88 m telescope of the National Astronomical Observatory of Japan (NAOJ) in Okayama, Japan. MuSCAT data were extracted using the custom pipeline described in (Fukui et al. 2011).

^g MuSCAT2 (Narita et al. 2019) 4-color multi-band simultaneous camera on the 1.52 m Telescopio Carlos S\'anchez (TCS). Data reduction follows Parviainen et al. (2019).

^h Fred L. Whipple Observatory / KeplerCam

ⁱ TUBITAK National Observatory (TUG)